Fisheye Camera Method for Determining Spatial Non-Uniformity Corrections in Luminous Flux Measurements with Integrating Spheres

Alexander Kokka

School of Electrical Engineering

Thesis submitted for examination for the degree of Master of Science in Technology.

Espoo 31.8.2016

Thesis supervisor:

Prof. Erkki Ikonen

Thesis advisors:

M.Sc. (Tech.) Tomi Pulli

D.Sc. (Tech.) Tuomas Poikonen

Aalto University
School of Electrical
Engineering

AALTO UNIVERSITY
SCHOOL OF ELECTRICAL ENGINEERING

ABSTRACT OF THE
MASTER'S THESIS

Author: Alexander Kokka

Title: Fisheye Camera Method for Determining Spatial Non-Uniformity Corrections in Luminous Flux Measurements with Integrating Spheres

Date: 31.8.2016 Language: English Number of pages: 7+52

Department of Signal Processing and Acoustics

Professorship: Measurement Science and Technology

Supervisor: Prof. Erkki Ikonen

Advisors: M.Sc. (Tech.) Tomi Pulli, D.Sc. (Tech.) Tuomas Poikonen

The energy efficiency of lighting products is described in terms of luminous efficacy. It is the ratio of the produced total luminous flux and the consumed active electrical power. Luminous flux, the total amount of visible light produced by a light source, as perceived by the human eye, is often measured with integrating sphere photometers. Low uncertainties in measurements with integrating spheres require a correction factor to account for the spatial non-uniformity of the sphere. Traditionally, obtaining this correction factor has required time consuming and resource intensive goniometric measurements of the relative angular intensity distribution of the lamp under test.

In this thesis, a fisheye camera method for determining spatial non-uniformity corrections in luminous flux measurements with integrating spheres is presented. Using a fisheye lens camera mounted into the detector port of an integrating sphere, the relative angular intensity distribution of a luminaire operated inside the sphere is resolved. The developed method does not require any modifications to the integrating sphere. To automate the measurement procedure, measurement and analysis software utilizing the method was developed.

The developed method and software were validated by measuring the relative angular intensity distributions of twelve LED lamps of different types using the fisheye camera method with two different grade camera modules and a goniophotometer for the reference. For the luminaires tested, the deviations between the spatial correction factors obtained using the two methods ranged from 0.01 % to 0.32 %, depending on the angular spread of the measured lamp. For the fisheye camera method and a typical LED lamp, the expanded uncertainty ($k = 2$) for the spatial non-uniformity correction factor was determined to be 0.28 %.

Keywords: Fisheye camera, Integrating sphere, Luminous flux, Spatial correction, Angular intensity distribution, Photometry, Measurement uncertainty

AALTO-YLIOPISTO
SÄHKÖTEKNIIKAN KORKEAKOULU

DIPLOMITYÖN
TIIVISTELMÄ

Tekijä: Alexander Kokka

Työn nimi: Kalansilmäkameramenetelmä spatiaalikorjauksien määrittämiseen valovirtamittauksille integroivassa pallossa

Päivämäärä: 31.8.2016 Kieli: Englanti Sivumäärä: 7+52

Signaalinkäsittelyn ja akustiikan laitos

Professuuri: Mittaustekniikka

Työn valvoja: Prof. Erkki Ikonen

Työn ohjaajat: DI Tomi Pulli, TkT Tuomas Poikonen

Valonlähteiden energiatehokkuutta kuvataan fotometrisella suureella valotehokkuus. Se määritellään lampun tuottaman valovirran ja kulutetun pätötehon suhteena. Valovirta eli ihmissilmän havaittavissa oleva lähteen tuottama kokonaisvalomäärä mitataan usein integroivalla pallofotometrillä. Pienen mittausepävärmuuden saavuttaminen integroivalla pallolla vaatii korjauskerrointa pallon epätasaisen spatiaalivasteen vuoksi. Perinteisesti käytetty menetelmä spatiaalikorjauskertoimen määrittämiseksi on vaatinut aikaavievää ja resursseja sitovaa goniometrimittausta testattavan valonlähteen intensiteettijakauman selvittämiseksi.

Tässä työssä esitellään spatiaalikorjauskertoimen määrittämiseksi kehitetty mittausmenetelmä, joka perustuu integroivan pallon kanssa käytettävään kalansilmäkameraan. Menetelmässä integroivan pallon ilmaisinporttiin asennetun kameran avulla määritetään pallossa olevan valaisimen suhteellinen intensiteettijakauma. Kehitetty menetelmä ei vaadi rakenteellisia muutoksia olemassaolevaan integroivaan palloon. Mittauksen automatisoimiseksi kehitettiin menetelmään perustuva mittaus- ja analysointiohjelma.

Kehitetyt menetelmä ja mittausohjelma validoitiin mittaamalla kahdentoista erilaisen LED-lampun suhteelliset intensiteettijakaumat käyttäen kalansilmäkameramenetelmää kahdella eri hintaluokan kameramoduulilla ja vertaamalla tuloksia goniofotometrillä saatuihin tuloksiin. Spatiaalikorjauskertoimet mitatuille lampuille poikkesivat näiden kahden menetelmän välillä 0,01–0,32 %. Kehitetyn kalansilmäkameramenetelmän laajennettu mittausepävarmuus ($k = 2$) spatiaalikorjauskertoimen määrittämisessä tyypilliselle LED-lampulle on 0,28 %.

Avainsanat: Kalansilmäkamera, Integroiva pallo, Valovirta, Spatiaalikorjaus, Intensiteettijakauma, Fotometria, Mittausepävarmuus

Preface

I would like to thank Professor Erkki Ikonen for supervising this thesis and for the opportunity to work on the subject. I would also like to thank my advisors M.Sc. (Tech.) Tomi Pulli and D.Sc. (Tech.) Tuomas Poikonen for sharing their expertise and all the encouragement. This gratitude extends to the whole team at the Metrology Research Institute and all the other professionals I have had a pleasure to work with in the past. Many thanks are also due to my friends and family for the endless support along these years. And I would also like to thank Laura. Thank you, Laura.

Otaniemi, 31.8.2016

Alexander Kokka

Contents

Symbols and abbreviations

Symbols

A	area of the precision aperture
$\boldsymbol{B}_{\mathrm{ch}}$	blue color channel
c	combination of the correction factors
E_{v}	illuminance
f	focal length, principal distance
F	spectral mismatch correction factor
$\boldsymbol{G}_{\mathrm{ch}}$	green color channel
i	photocurrent
$I_{\mathrm{v}}(\theta, \phi)$	relative angular intensity distribution
k_{a}	correction factor for illuminance non-uniformity
k_{s}	spatial non-uniformity correction factor
$K(\theta, \phi)$	spatial responsivity distribution function (SRDF)
K_{m}	photopic normalization constant
$\boldsymbol{K}$	intrinsic parameter matrix
$\boldsymbol{M}$	projection matrix
(o_x, o_y)	principal point in the pixel coordinate system
p	point in the image plane coordinate system
p_{i}	point in the pixel coordinate system
P	active electrical power
${}^{\mathrm{c}}\boldsymbol{P}$	point in the camera coordinate system
${}^{\mathrm{w}}\boldsymbol{P}$	point in the world coordinate system
r_{d}	distorted radial distance from the image center
r_{u}	undistorted radial distance from the image center
R_{s}	sphere radius
$\boldsymbol{R}$	rotation matrix
$\boldsymbol{R}_{\mathrm{ch}}$	red color channel
$\boldsymbol{t}$	translation vector
s_x	pixel x dimension
s_y	pixel y dimension
$\boldsymbol{T}$	extrinsic parameter matrix
$V(\lambda)$	relative spectral sensitivity of human eye
x	x coordinate in the image plane coordinate system
x_{i}	x coordinate in the pixel coordinate system
X	x coordinate in the camera coordinate system
${}^{\mathrm{w}}X$	x coordinate in the world coordinate system
y	y coordinate in the image plane coordinate system
y_{i}	y coordinate in the image plane coordinate system
Y	y coordinate in the camera coordinate system
$\boldsymbol{Y}$	pixel intensity matrix
${}^{\mathrm{w}}Y$	y coordinate in the world coordinate system
Z	z coordinate in the camera coordinate system
${}^{\mathrm{w}}Z$	z coordinate in the world coordinate system

α_c	pitch angle of the camera
β	correction factor for the incident angle
β_c	yaw angle of the camera
γ	skew coefficient
γ_c	roll angle of the camera
η_v	luminous efficacy
θ	zenith angle in the world coordinate system
θ_DUT	deviation angle from the central beam
θ_oa	deviation angle from the optical axis of the camera (incident)
θ'_oa	deviation angle from the optical axis of the camera (deflected)
λ	wavelength
σ	standard deviation
ϕ	azimuth angle in the world coordinate system
ϕ_DUT	rotation angle about the main axis of the lamp
ϕ_oa	rotation angle about the optical axis of the camera
$\Phi_{\mathrm{e},\lambda}(\lambda)$	spectral radiant flux
Φ_v	luminous flux

Abbreviations

AC	alternating current
ADC	analog-to-digital converter
$BaSO_4$	barium sulfate
CIE	Commission Internationale de l'Éclairage (International Commission on Illumination)
CLI	command line interface
DUT	device under test
FOV	field of view
GUI	graphical user interface
LED	light emitting diode
MRI	Metrology Research Institute
NIST	National Institute of Standards and Technology
NMI	National Metrology Institute
PEP	Python Enhancement Proposal
PLC	power line cycle
POM	polyoxymethylene
RGB	red, green, and blue (color model)
SNR	signal-to-noise ratio
SSL	solid-state lamp
SRDF	spatial responsivity distribution function
USB	universal serial bus

1 Introduction

The luminous efficacy of an electrical light source describes the ratio of the produced total luminous flux and the consumed active electrical power. Luminous flux is the measure of visible light, weighted by the spectral sensitivity of the human eye. Because of the vast amount of globally utilized electrical lighting, even small differences in luminous efficacy values can lead to a large total of gained, or wasted energy. Furthermore, a large measurement uncertainty of luminous efficacy during research and development phase can lead to the development of inferior lighting products at the expense of superior ones. Therefore, the ability to accurately measure luminous efficacy at test laboratories is of paramount importance.

One of the methods used for measuring the luminous flux emitted by a light source is the absolute integrating sphere method. To reach low uncertainties with this method, several corrections need to be applied to the results [1]. Applying some of these corrections is time consuming and resource intensive, and therefore mainly available for National Metrology Institutes (NMIs). An example of the more resource intensive correction is the spatial non-uniformity correction that requires knowledge of both the spatial uniformity of the integrating sphere, measured with a sphere scanner, and the angular light distribution of the source, traditionally measured with a goniophotometer. Increasing popularity of solid state lamps (SSLs), such as light emitting diode (LED) based luminaires, highlights the necessity to efficiently apply these corrections because of the wide variety of angular intensity distributions of SSLs compared to incandescent light sources.

In this thesis, the absolute integrating sphere method is modified to use a fisheye lens camera installed into the detector port of an integrating sphere to make up for the conventional angular intensity distribution measurement setup. The developed method is intended to enable industrial test laboratories to apply spatial non-uniformity corrections in order to lower the uncertainty of luminous efficacy measurements, without any need for modifications to their existing measurement equipment. The original idea for the spatial non-uniformity corrections using fisheye cameras in measurements with integrating spheres comes from the work by Y. Zong at the National Institute of Standards and Technology (NIST) [2].

The theory part of the thesis is twofold. In Section 2, the traditional absolute integrating sphere method is introduced. The main focus of the section is on the elements required for determining the spatial non-uniformity correction factor. Section 3 concentrates on the image formation geometry and the mathematical camera models needed for resolving relative angular intensity distributions of luminaires from fisheye lens camera images.

In Section 4, the developed fisheye camera method is presented. After an overview, the method is detailed starting with the technical characteristics of the employed imaging hardware and its geometric calibration procedure, along with the mechanical

design of an adapter used to mount the camera to the detector port of the sphere used at the Metrology Research Institute (MRI). In addition to applying the camera theory introduced in Section 3, the image processing and analysis techniques utilized in the method are explained. The section is concluded by a walkthrough of the developed software for automated measurements and result analysis.

In Section 5, a validation procedure for the method and the results of the validation are discussed. The relative angular intensity distributions obtained using the developed method are presented and compared to their respective goniophotometer references. Also, in this section, the impact of the deviations between the methods on the spatial correction, and correspondingly the luminous efficacy, is studied – along with the uncertainty analysis of the spatial non-uniformity correction factor obtained using the developed fisheye camera method. The work is concluded in Section 6.

2 Absolute integrating sphere method

In this chapter, the absolute integrating sphere method is introduced. First, the definition of luminous efficacy and an overview of the method are presented. This is followed by a detailed review of the factors inflicting spatial non-uniformities and the goniometric method used to reduce the measurement uncertainty due to them. In the last part of the chapter, the correction factors of the absolute integrating sphere method are discussed – most prominently the spatial correction, which is the main focus of the developed fisheye camera method.

2.1 Luminous efficacy

The luminous efficacy describes the energy efficiency of a light source and is defined as a ratio [3]

$$\eta_\mathrm{v} = \frac{\Phi_\mathrm{v}}{P}\,, \tag{1}$$

where Φ_v is the total luminous flux (unit lumen, lm) and P is the active electrical power consumption (unit watt, W) of the luminaire.

The total luminous flux is a photometric quantity describing the total amount of visible light emitted by a light source. It equals to radiometric quantity spectral radiant flux $\Phi_{\mathrm{e},\lambda}(\lambda)$ (unit watt, W) weighted by the spectral luminous efficiency function for photopic vision $V(\lambda)$ [3]. The $V(\lambda)$ curve is shown in Figure 1.

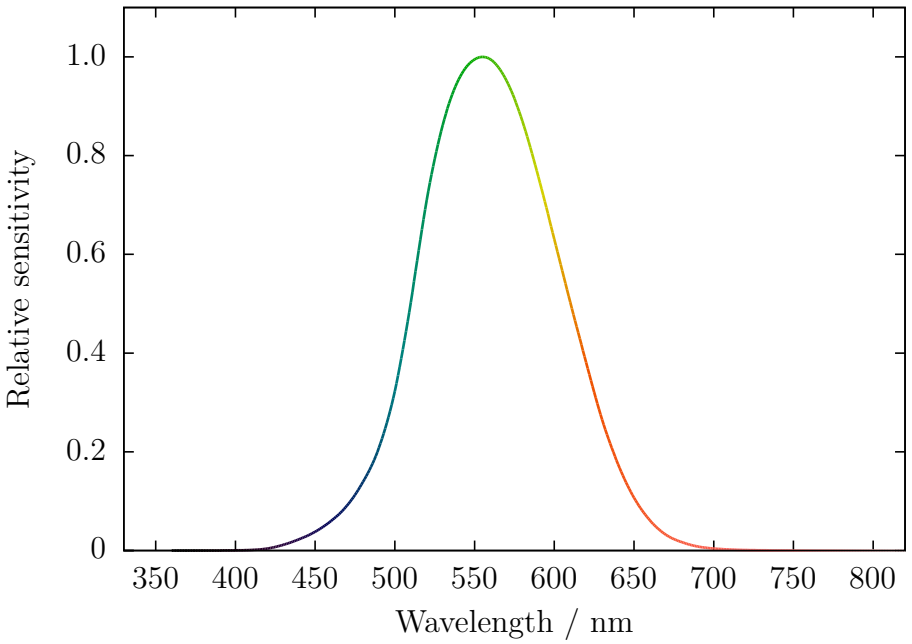

Figure 1: The relative spectral sensitivity of the human eye in well-lit, or photopic, conditions as defined by the CIE. The line color corresponds to the perceived color.

The $V(\lambda)$ function models the sensitivity of the human vision to electromagnetic radiation at different wavelengths. The International Commission on Illumination (Commission Internationale de l'Éclairage, CIE) defines the $V(\lambda)$ function to be non-zero in the wavelength region from 360 to 830 nm, and to have a peak value at 555 nm of the spectrum which is perceived as a green color. By using $V(\lambda)$, any radiometric quantity $X_{\mathrm{e},\lambda}(\lambda)$ can be transformed into the respective photometric quantity by

$$X_{\mathrm{v}} = K_{\mathrm{m}} \int_{360\,\mathrm{nm}}^{830\,\mathrm{nm}} V(\lambda) X_{\mathrm{e},\lambda}(\lambda)\,\mathrm{d}\lambda\,, \tag{2}$$

where K_{m} is a normalization constant 683 lm/W. [3]

Photometric quantities can also be measured directly using a photometer. Photometer is a detector whose spectral responsivity mimics the shape of $V(\lambda)$ function. Thus its output is already weighted as a photometric quantity.

2.2 Principle of the absolute integrating sphere method

Ideally, the total luminous flux $\Phi_{\mathrm{v,DUT}}$ of a device under test (DUT), mounted inside a uniformly reflective, spectrally non-selective enclosure and measured with a baffled photometer, is directly proportional to the photocurrent of the detector $\Phi_{\mathrm{v,DUT}} \propto i_{\mathrm{DUT}}$ [4]. By introducing a known amount of luminous flux Φ_{ref} into the enclosure as a reference and measuring the resulting photocurrent i_{ref}, the absolute value of $\Phi_{\mathrm{v,DUT}}$ can subsequently be determined using

$$\frac{\Phi_{\mathrm{v,DUT}}}{\Phi_{\mathrm{ref}}} = \frac{i_{\mathrm{DUT}}}{i_{\mathrm{ref}}}\,. \tag{3}$$

In practice, to obtain the total luminous flux of a lighting product, the ratio of the photometer signals needs to be adjusted using a combined correction coefficient c according to equation

$$\Phi_{\mathrm{v,DUT}} = c\,\frac{i_{\mathrm{DUT}}}{i_{\mathrm{ref}}}\,\Phi_{\mathrm{ref}}\,, \tag{4}$$

which compensates for the non-ideal properties of the measurement system. The correction coefficient c consists of several components and can be written as

$$c = \frac{k_{\mathrm{s}} F k_{\mathrm{a}}}{\beta}\,. \tag{5}$$

It includes correction factors for spatial non-uniformity k_{s}, spectral mismatch F, illuminance non-uniformity of the reference source k_{a}, and the angle of incidence of the reference luminous flux β. [1, 4]

The spatial non-uniformity correction factor k_{s}, which is one of the key elements of the correction coefficient c, requires knowledge on the spatial responsivity of the

enclosure and the relative angular intensity distribution of the device under test [1]. These two elements will be discussed next, along with the luminous flux measurement setup at the MRI, before returning to the correction coefficient c in Section 2.5.

2.3 Spatial responsivity of integrating spheres

In the absolute integrating sphere method, the relative luminous flux of the DUT is determined by operating the lamp inside an integrating sphere. An ideal integrating sphere is a hollow sphere which is made of, or coated with, a diffusely reflective, spectrally non-selective material which is spatially uniform along the inner surface of the sphere [3]. The illuminance at any point of that surface, which is not exposed to the direct flux of the lamp, is proportional to the luminous flux produced inside the sphere, or introduced into the sphere through an aperture [1, 4, 5]. A 3D model based on the integrating sphere used at the MRI is presented in Figure 2.

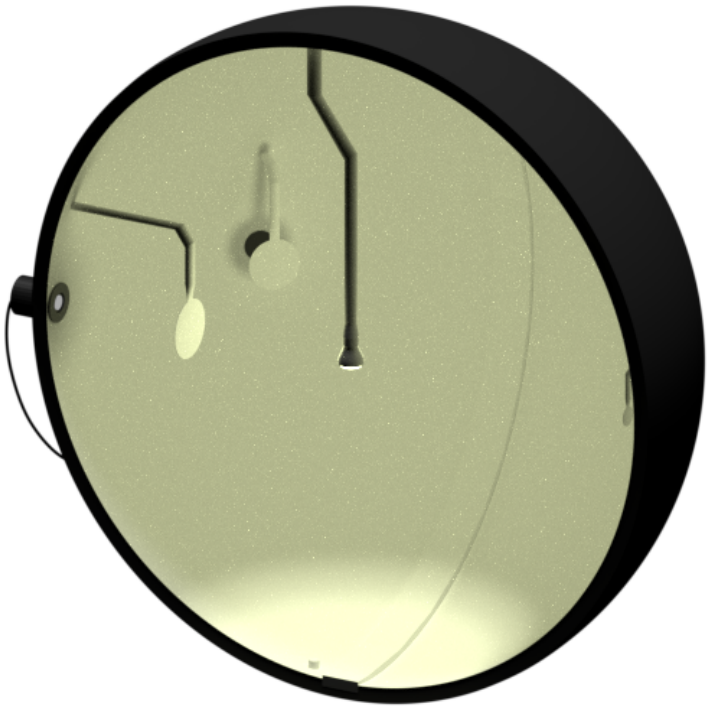

Figure 2: The cross section of an integrating sphere model based on the sphere used at the MRI. A spot type DUT is installed in the E27-base lamp holder. The sphere opens up in the perpendicular direction to the cross section.

In reality, integrating spheres are never spatially uniform. Common elements causing spatial non-uniformity in a typical integrating sphere for luminous flux measurements consist of a detector port and its shading baffle, a lamp holder, and a seam between the two halves of the sphere. The sphere in Figure 2 is also equipped with a port for an external light source, a mounting socket for an alternative lamp

holder at the bottom, and an auxiliary port on the opposite side from the detector port. Aside from the aforementioned structural elements, additional spatial non-uniformity is induced by the varying reflectance of the inner surface of the sphere caused by uneven thickness of the coating and possible contamination factors [6].

The integrating sphere used at the MRI is 1.65 m in diameter and is coated with white barium sulfate ($BaSO_4$) paint that has approximately 98 % reflectivity in the visible region [4]. The spatial non-uniformity characteristics of the integrating sphere are visualized in Figure 3 using a map of the spatial responsivity distribution function (SRDF) $K(\theta, \phi)$, where θ and ϕ are the zenith and azimuth angles of the spherical coordinate system, respectively. The SRDF in Figure 3 was measured using a commercial sphere scanner [7].

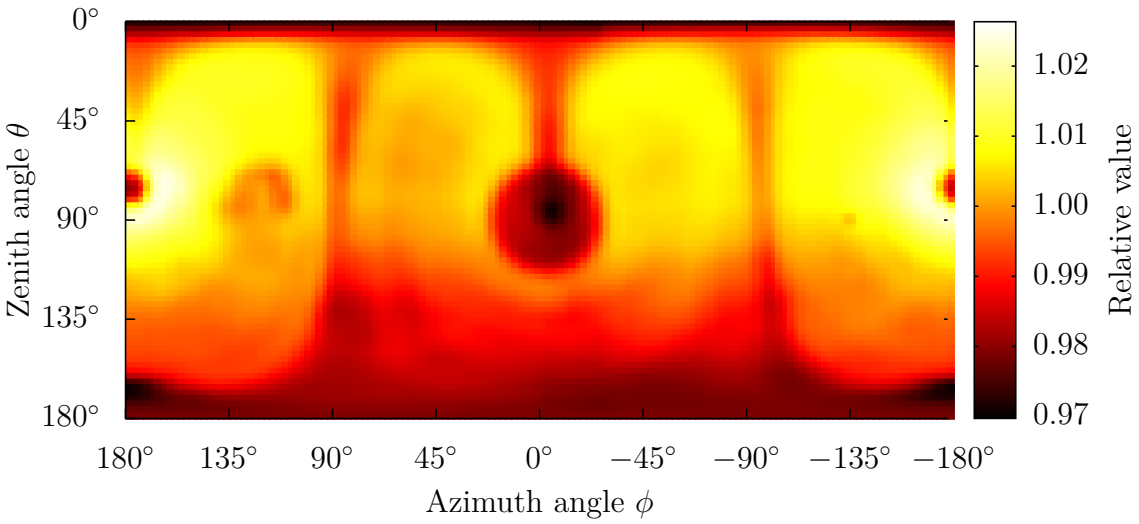

Figure 3: The SRDF $K(\theta, \phi)$ of the integrating sphere at the MRI. The auxiliary port is located at $\{\theta = 90°, \phi = 0°\}$.

Because of the equirectangular projection of the map in Figure 3, areas diverging from $\theta = 90°$ appear over-represented. The effect of some distinct structural features on the luminous responsivity of the integrating sphere can be identified from the SRDF map:

- the auxiliary port $\{90°, 0°\}$
- the detector port $\{90°, 180°\}$ and $\{90°, -180°\}$
- the external port $\{90°, 135°\}$
- the socket for an alternative lamp holder $\{165°, 180°\}$ and $\{165°, -180°\}$
- the seam of the two halves of the sphere $\phi = 90°$ and $\phi = -90°$.

The correspondence of the SRDF map and the full measurement setup can be seen in Figure 4. In addition to the aforementioned integrating sphere, the setup consists of a reference source and its aperture array, a standard photometer, and the detector for the DUT. The reference luminous flux is produced by utilizing the average illuminance E_v of a reference source over a precision aperture area A outside the sphere and can be obtained as [4]

$$\Phi_\mathrm{ref} = E_\mathrm{v} A \,. \tag{6}$$

The center of the luminous flux of the reference source Φ_ref, introduced through the external port at $\{90°, 135°\}$, has its first reflection on the inner surface of the sphere at $\{\theta_\mathrm{ref}, \phi_\mathrm{ref}\} = \{90°, 45°\}$.

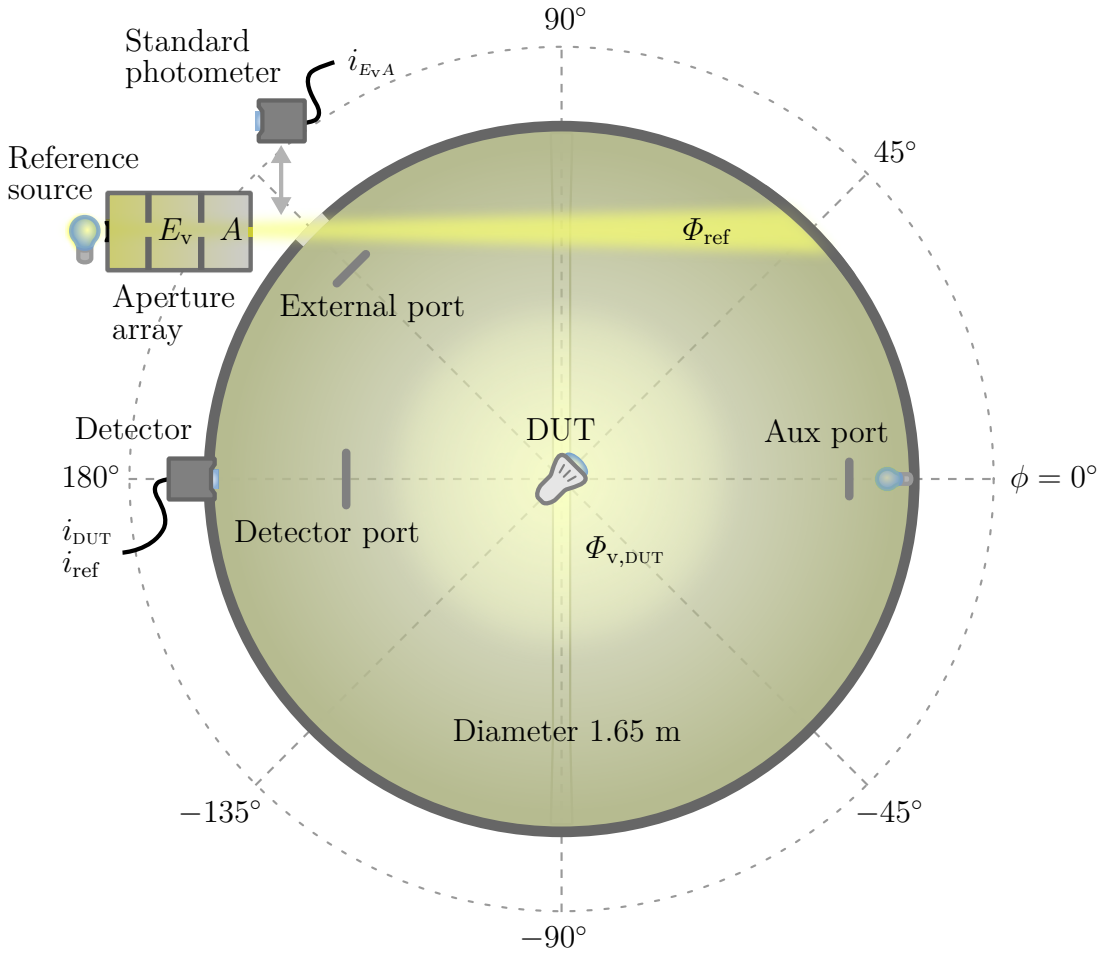

Figure 4: A top view schematic of the luminous flux measurement setup at the MRI. During measurements, the DUT and the reference source are operated alternately. Except for the seam of the sphere, all the pictured elements reside at $\theta \approx 90°$.

2.4 Angular intensity distribution

In addition to the spatial responsivity distribution of the integrating sphere, calculation of the spatial non-uniformity correction factor k_s requires determining the relative angular intensity distribution $I_v(\theta, \phi)$ of the device under test. This comes from the necessity to know which areas of the inner surface of the sphere are illuminated by the direct luminous flux emitted by the luminaire.

In most cases, luminaires can be divided into two groups based on their angular intensity distributions: spot and bulb types. A lamp can be considered to be a spot lamp when majority of its luminous flux is directed into one hemisphere. Two important parameters describing the angular intensity distribution of a spot type lamp are the central beam intensity and beam angle. The beam angle is defined as an angle of full width at half maximum in relation to the central beam intensity.

Traditionally, goniophotometers are used to determine angular intensity distributions of light sources. Such a measurement setup consists of a detector and positioning equipment for the DUT or the detector, or both. Also, light from other sources than the DUT must be prevented from disturbing the measurement.

The near-field goniophotometer used at the MRI is schematically illustrated in Figure 5. The positioning system consists of two motorized rotary stages which turn the device under test horizontally θ_{DUT} and about its mechanical axis ϕ_{DUT}. For each position of the lamp, the signal of the photometer is integrated over a predetermined number of power line cycles (PLCs) to reduce the effect of the flicker caused by alternating current (AC) of the power supply. The purpose of the aperture box is to block any straylight caused by the reflected light of the DUT and luminous flux from any other light sources. The distance between the DUT and the detector is approximately 1.3 m. The system is operated in a dark room.

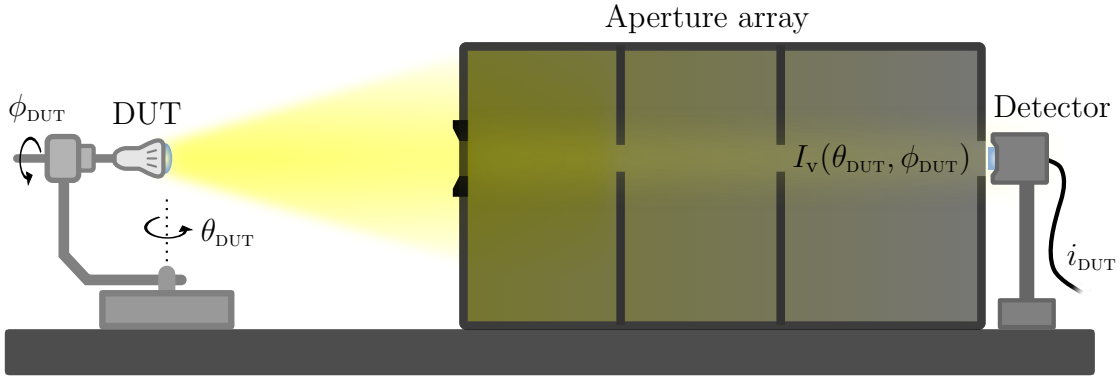

Figure 5: A schematic representation of the goniophotometer setup at the MRI. The flank of the aperture box is made semitransparent for the demonstration purposes.

In addition to the requirement of a dark room and costly positioning equipment, the angular intensity distribution measurement procedure can be very time consuming

depending on the radiation pattern of the luminaire and the angular resolution of the scan ($\Delta\theta_{\mathrm{DUT}}, \Delta\phi_{\mathrm{DUT}}$). For instance, one photometric scan of a hemisphere with a moderate resolution of ($\Delta\theta_{\mathrm{DUT}} = 5°, \Delta\phi_{\mathrm{DUT}} = 5°$) takes several hours, depending on the type of the lamp, in addition to the time which it takes for the DUT to stabilize.

2.5 Correction factors

The factor for the spatial non-uniformity correction k_{s} of the correction coefficient c in equation 5 consists of the spatial correction elements for the device under test and the reference source introduced through the external port of the integrating sphere. It is given by

$$k_{\mathrm{s}} = \frac{\int_{\phi}\int_{\theta} K(\theta_{\mathrm{ref}}, \phi_{\mathrm{ref}})\, I_{\mathrm{v}}(\theta, \phi)\, \sin(\theta)\, \mathrm{d}\theta\, \mathrm{d}\phi}{\int_{\phi}\int_{\theta} K(\theta, \phi)\, I_{\mathrm{v}}(\theta, \phi)\, \sin(\theta)\, \mathrm{d}\theta\, \mathrm{d}\phi}\,, \tag{7}$$

where $\sin(\theta)$ weighting is used to compensate the over-represented areas of zenith angles $\theta \neq 90°$ due to the spherical coordinate system (see Figure 3) [8]. $K(\theta_{\mathrm{ref}}, \phi_{\mathrm{ref}})$ is the spatial responsivity of the integrating sphere wall location directly illuminated by the luminous flux from the reference source.

Due to the possible mechanical imperfections, such as inclined lamp holder, lamps with deviating optical and mechanical axes, and the matter of unpredictable ϕ_{DUT} alignment in the lamp holder of the sphere, the angular intensity distribution inside the sphere $I_{\mathrm{v}}(\theta, \phi)$ may not accurately coincide with the measured $I_{\mathrm{v}}(\theta_{\mathrm{DUT}}, \phi_{\mathrm{DUT}})$. Fortunately, for some luminaires, the spatial non-uniformity correction is not sensitive to small deviations in the relative angular intensity distribution, and often luminaires of the same type can be represented by angular intensity distribution data of just one lamp [1].

Spectral mismatch correction F needs to be applied when the radiation spectrum of the reference source differs from the one of the device under test. The factor also includes corrections due to the spectral selectivity of the inner surface of the sphere and spectral responsivity deviation of the sphere photometer from the $V(\lambda)$. [9]

The correction factor for angle of incidence of the reference source β takes into account the difference in incident angles of the sources. For instance, in the integrating sphere at the MRI, the luminous flux from a reference source Φ_{ref}, introduced into the sphere through the external port of the sphere, has its first reflection from the sphere wall at the angle of 45° while the flux from a luminaire inside the sphere has a normal incidence (see Figure 4). [4]

The precision aperture area A is not illuminated uniformly by the reference source. This is due to the geometry of the light source and the relatively short distance of the luminaire to the aperture. Thus the correction factor k_{a} is needed to adjust the measured value of the luminous flux Φ_{ref} produced by the reference source. [4]

3 Perspective and fisheye camera models

In this section, the underlying theory of fisheye lens cameras is discussed. First, the imaging geometry and the pinhole camera model are introduced. The pinhole camera serves as a foundation for the following fisheye camera model, which additionally incorporates extreme radial lens distortion. Different fisheye lens projection geometries are discussed in the end of the chapter.

3.1 Geometric image formation overview

Geometric digital image formation is essentially a projection of a scene, or the world points, into the respective pixel coordinates. This operation can be broken down into three separate transitions between four different coordinate systems. All the coordinate systems and their corresponding point notations are presented in Table 1. Geometric image formation follows the order from top to bottom of the table. The direction of a possible back projection from an image to the scene is accordingly from bottom to top.

Table 1: Coordinate systems used in geometric image formation

Coordinate system	Point notation	Coordinates
World	${}^{\mathrm{W}}\boldsymbol{P}$	${}^{\mathrm{W}}X$, ${}^{\mathrm{W}}Y$, ${}^{\mathrm{W}}Z$
Camera	${}^{\mathrm{C}}\boldsymbol{P}$	X, Y, Z
Image plane	p	x, y
Pixel	p_{i}	$x_{\mathrm{i}}, y_{\mathrm{i}}$

The Cartesian world coordinate system origin coincides with the spherical one at the center of the sphere $(r, \theta, \phi) = (0, 0, 0) = ({}^{\mathrm{W}}X_0, {}^{\mathrm{W}}Y_0, {}^{\mathrm{W}}Z_0) = {}^{\mathrm{W}}\boldsymbol{P}_0$ with the positive z axis corresponding to $\theta = 0$. The origin of the camera coordinate system ${}^{\mathrm{C}}\boldsymbol{P}_0$ lies at the center of projection, or the aperture of the pinhole camera. This is also the location of the camera model in the world coordinate system ${}^{\mathrm{W}}\boldsymbol{P}_{\mathrm{C}}$.

A visualization of the geometry of the coordinate systems is shown in Figure 6. The spherical coordinates of the figure are consistent with the coordinates used in the schematic illustration of the integrating sphere in Figure 4. The origin of the camera coordinate system resides at the location of the detector port of the integrating sphere.

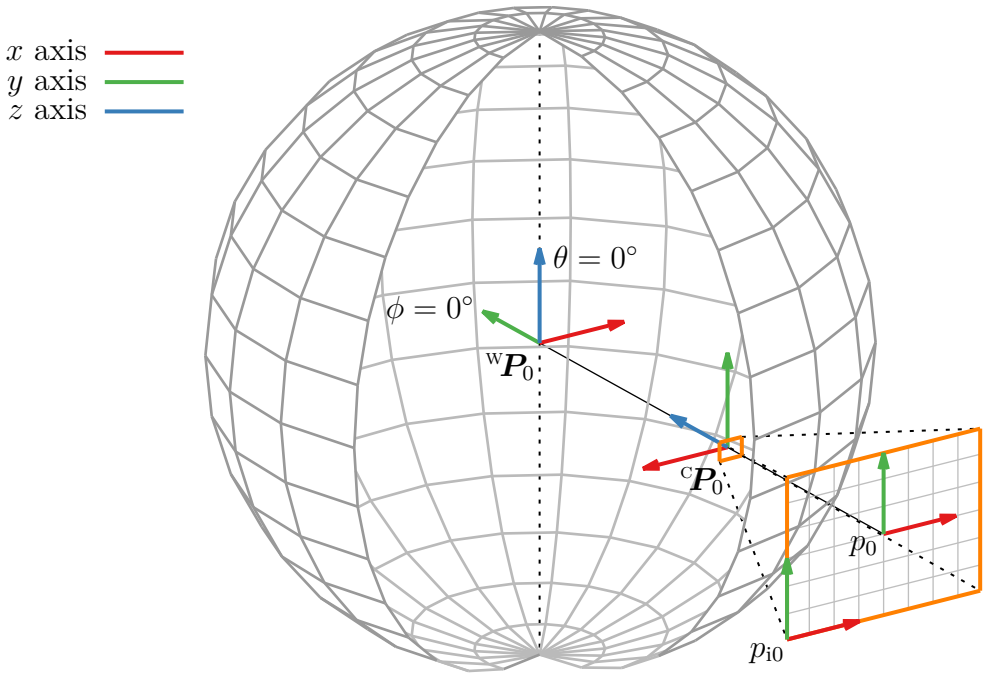

Figure 6: The world, camera, image plane, and pixel coordinate systems for a sphere with a camera at $\{\theta = 90°, \phi = 180°\}$.

The z axis of the camera coordinate system is parallel to the optical axis of the camera and perpendicular to the image sensor. The x axis is parallel with the horizontal and the y axis with the vertical edge of the sensor. In practice, because of mechanical non-idealities, the orthogonal geometry between the world and camera coordinate systems shown in Figure 6 is difficult to realize.

The image plane lies on the negative z axis of the camera coordinate system. The x and y axes of image plane are parallel to x and y axes of the camera coordinate system respectively, but the x axes are oppositely directed. The origin of the image plane p_0, which is also called the principal point, lies at the intersection of the image plane and the optical axis of the camera.

The pixel coordinate system is situated on the image plane but is discrete, and the origin is shifted to the corner of the image sensor so that there are no negative pixel coordinate values. The pixel resolution of the image sensor determines the resolution of the pixel coordinate system (8×6 in Figure 6).

3.2 Rigid transformation

Since the camera is not situated at the world coordinate system origin, the coordinates of every world point ${}^{\mathrm{W}}\boldsymbol{P} = \begin{pmatrix} {}^{\mathrm{W}}X & {}^{\mathrm{W}}Y & {}^{\mathrm{W}}Z \end{pmatrix}^{\mathrm{T}}$ need first to be transformed into the camera coordinate system. The corresponding camera coordinate system point

${}^{\mathrm{C}}\boldsymbol{P} = \begin{pmatrix} X & Y & Z \end{pmatrix}^{\mathrm{T}}$ can be calculated using the rotation matrix $\boldsymbol{R}$ and the translation vector $\boldsymbol{t}$ [10]

$$ {}^{\mathrm{C}}\boldsymbol{P} = \boldsymbol{R}\,{}^{\mathrm{W}}\boldsymbol{P} + \boldsymbol{t} = \begin{bmatrix} R_{11} & R_{12} & R_{13} \\ R_{21} & R_{22} & R_{23} \\ R_{31} & R_{32} & R_{33} \end{bmatrix} \begin{pmatrix} {}^{\mathrm{W}}X \\ {}^{\mathrm{W}}Y \\ {}^{\mathrm{W}}Z \end{pmatrix} + \begin{pmatrix} t_1 \\ t_2 \\ t_3 \end{pmatrix}. \tag{8} $$

The rotation matrix and the translation vector represent the pose of the camera with respect to the world coordinate system origin. In the simple case of the orthogonal geometry in Figure 6, the transformation equation is

$$ {}^{\mathrm{C}}\boldsymbol{P} = \begin{bmatrix} -1 & 0 & 0 \\ 0 & 0 & 1 \\ 0 & 1 & 0 \end{bmatrix} \begin{pmatrix} {}^{\mathrm{W}}X \\ {}^{\mathrm{W}}Y \\ {}^{\mathrm{W}}Z \end{pmatrix} + \begin{pmatrix} 0 \\ -R_{\mathrm{s}} \\ 0 \end{pmatrix}, \tag{9} $$

where R_{s} is the radius of the sphere. For each point, the whole operation can be combined into a single homogeneous transformation by the 4×4 extrinsic parameter matrix $\boldsymbol{T}$ which fully describes the position of the world point with respect to the camera according to

$$ \begin{pmatrix} {}^{\mathrm{C}}\boldsymbol{P} \\ 1 \end{pmatrix} = \begin{pmatrix} X \\ Y \\ Z \\ 1 \end{pmatrix} = \underbrace{\begin{bmatrix} R_{11} & R_{12} & R_{13} & t_1 \\ R_{21} & R_{22} & R_{23} & t_2 \\ R_{31} & R_{32} & R_{33} & t_3 \\ 0 & 0 & 0 & 1 \end{bmatrix}}_{\boldsymbol{T}} \begin{pmatrix} {}^{\mathrm{W}}X \\ {}^{\mathrm{W}}Y \\ {}^{\mathrm{W}}Z \\ 1 \end{pmatrix} = \left[\begin{array}{c|c} \boldsymbol{R} & \boldsymbol{t} \\ \hline 0 & 1 \end{array}\right] \begin{pmatrix} {}^{\mathrm{W}}\boldsymbol{P} \\ 1 \end{pmatrix}. \tag{10} $$

3.3 Perspective camera model

The most fundamental camera model for the perspective projection is the pinhole camera model [11]. The model neglects all optical distortions, maintains straight lines, and can be simply modeled by the perspective projection and a single affine transformation which is the rotation of 180° about the optical axis. The pinhole camera model maps a three dimensional camera coordinate system point ${}^{\mathrm{C}}\boldsymbol{P}$ to a respective image plane coordinate point $p = (x, y)$ according to

$$ x = \quad f\frac{X}{Z} \quad \text{and} \tag{11} $$

$$ y = -f\frac{Y}{Z}, \tag{12} $$

where f is the focal length of the camera, which is the distance between the center of projection and the image plane [11]. The resulting image is mirrored about the optical axis. The minus sign in equation (12) indicates that points from positive y axis in the camera coordinate system get projected on the negative y axis on the

image plane. Because the x axes are oppositely directed, no negation occurs. The pinhole camera model is presented in Figure 7.

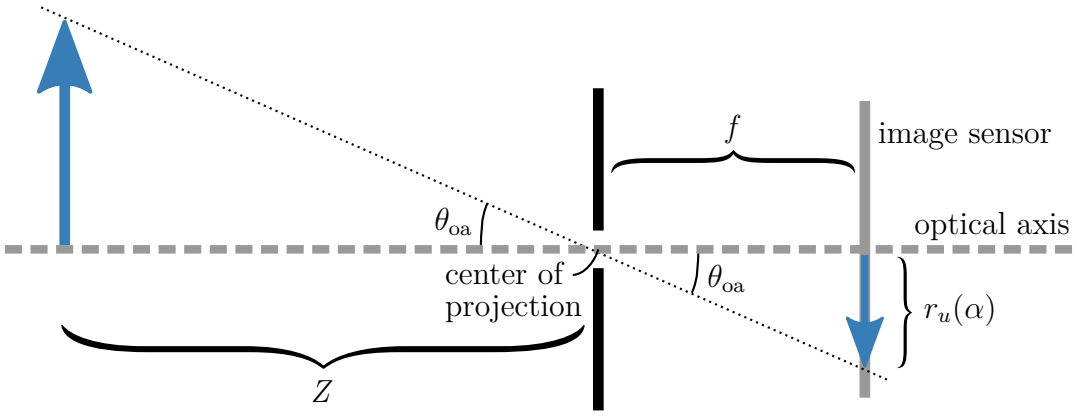

Figure 7: The pinhole camera model. In case of an ideal pinhole camera, the incident and the deflected angles are the same. The arrow on the left hand side is projected without any distortions.

For a projected point $p = (x, y)$, the radial distance $r_{\mathrm{u}}(x, y) = \sqrt{x^2 + y^2}$ from the principal point $p_0 = (x_0, y_0)$ is determined by the rectilinear projection mapping function [10]

$$r_{\mathrm{u}}(\theta_{\mathrm{oa}}) = f \tan(\theta_{\mathrm{oa}}) \,. \tag{13}$$

The subscript "u" denotes that the projection is undistorted. Because of the limited size of the image sensor of the camera, the projection distance proportional to the tangent of the incident angle quickly causes objects far enough from the optical axis to be projected outside the boundaries of the sensor.

The pixel coordinates $p_{\mathrm{i}} = (x_{\mathrm{i}}, y_{\mathrm{i}})$ corresponding to the coordinates of point p on the image plane can be obtained using equations

$$x_{\mathrm{i}} = \frac{(x - x_0)}{s_x} + o_x \quad \text{and} \tag{14}$$

$$y_{\mathrm{i}} = \frac{(y - y_0)}{s_y} + o_y \,, \tag{15}$$

where s_x and s_y are x and y dimensions of the sensor pixels and (o_x, o_y) is the principal point in the pixel coordinates. In case of the aligned camera and image coordinate system origins, x_0 and y_0 are both zero.

The aforementioned parameters f, o_x, o_y, s_x, and s_y, along with the skew coefficient γ, form the internal or intrinsic parameters of the camera [12]. The intrinsic parameters can be presented in the matrix form

$$\boldsymbol{K} = \begin{bmatrix} f/s_x & \gamma & o_x \\ 0 & -f/s_y & o_y \\ 0 & 0 & 1 \end{bmatrix}. \tag{16}$$

The skew coefficient γ is non-zero if pixel coordinate axes x and y are not orthogonal to each other. For modern cameras, the assumption of zero skew is well satisfied [13]. Thus using the matrix $\boldsymbol{K}$, the projection of a point ${}^{\mathrm{C}}\boldsymbol{P}$ to the image pixel coordinates can be written as

$$\begin{pmatrix} Z \cdot x_{\mathrm{i}} \\ Z \cdot y_{\mathrm{i}} \\ Z \end{pmatrix} = \begin{bmatrix} f/s_x & 0 & o_x \\ 0 & -f/s_y & o_y \\ 0 & 0 & 1 \end{bmatrix} \begin{pmatrix} X \\ Y \\ Z \end{pmatrix} = \boldsymbol{K}\,{}^{\mathrm{C}}\boldsymbol{P}. \tag{17}$$

The subsequent division of the left side of the equation by Z, to obtain the respective pixel coordinates, discards the depth data of the scene.

Finally, both the intrinsic and extrinsic parameters can be combined into a single 3×4 projection matrix $\boldsymbol{M}$ which solely describes the projection of any world coordinate system point ${}^{\mathrm{W}}\boldsymbol{P}$ to the camera pixel coordinates [12]

$$Z \cdot \begin{pmatrix} x_{\mathrm{i}} \\ y_{\mathrm{i}} \\ 1 \end{pmatrix} = \boldsymbol{K} \left[\begin{array}{c|c} \boldsymbol{R} & \boldsymbol{t} \end{array} \right] \begin{pmatrix} {}^{\mathrm{W}}X \\ {}^{\mathrm{W}}Y \\ {}^{\mathrm{W}}Z \\ 1 \end{pmatrix} = \boldsymbol{M} \begin{pmatrix} {}^{\mathrm{W}}\boldsymbol{P} \\ 1 \end{pmatrix}. \tag{18}$$

Because of the combination of the intrinsic and extrinsic parameters of the camera, the matrix $\boldsymbol{M}$ is often also called the camera matrix.

3.4 Fisheye camera model

3.4.1 Principle

Fisheye cameras are designed to produce images that cover a large portion of a hemispherical field, in some cases extending beyond the 180° field of view (FOV). The large FOV is achieved by utilizing lens systems with radial lens distortion which refract light coming from the incident angle θ_{oa} to the smaller deflection angle θ'_{oa} [14]. This contrasts with the pinhole camera model where incident and deflected angles are the same. The principle of fisheye lens camera is illustrated in Figure 8. Tangential distortions, which are perpendicular to the radial distortion, are generally negligible and do not require consideration [15, 16].

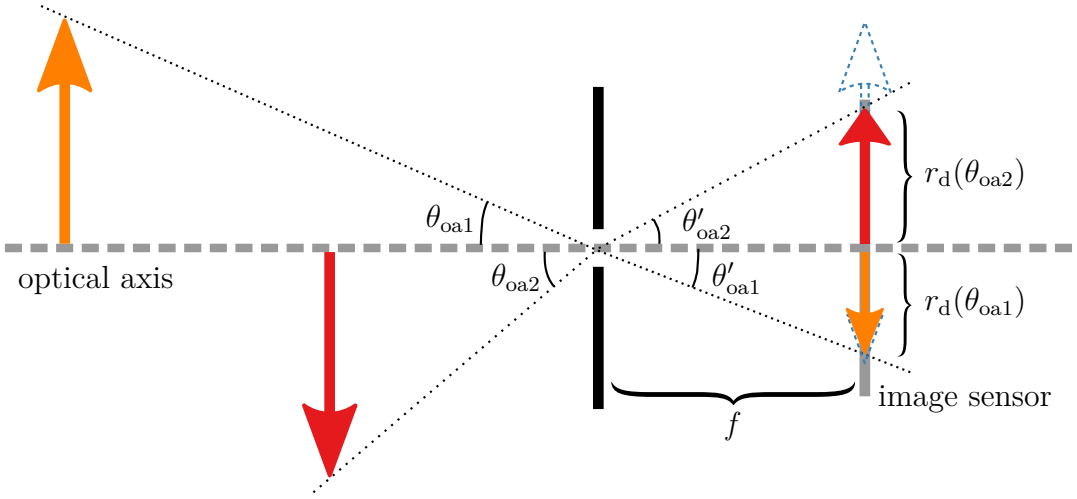

Figure 8: The geometrical model of fisheye camera. The blue dashed arrowheads correspond to the rectilinear projection. The subscript "d" stands for distorted.

The larger the incident angle, the more distorted is the projection on the image plane. This is depicted as the more deformed shape of the arrowhead with the larger incident angle in Figure 8. Points which lie on the optical axis are projected without distortion. The lens distortion can be considered as an additional layer in the geometric image formation. This layer is between the transition from the camera coordinate system point ${}^{C}\boldsymbol{P}$ to the image plane coordinate system point p.

3.4.2 Projection functions of fisheye lenses

There are various projection geometries for fisheye lenses. The geometries can be modeled by using the respective ideal projection functions of the lenses, or by using estimated radial lens models which include correction factors for imperfections [17]. In addition to projection geometries, lenses also differ in the way the image circle fills the image sensor.

In Figure 9, two image circle extremities, circular and full-frame projection, are shown. The circular projection fits the whole image circle on the image sensor but effectively reduces pixel resolution of the system by leaving a part of the sensor unused. On the other hand, full frame lens fills the whole sensor but subsequently omits the data from the peripheries of the image circle and thus decreases the field of view of the imaging system. The projection of a lens can also fall anywhere in between (a) and (b) in Figure 9. [18]

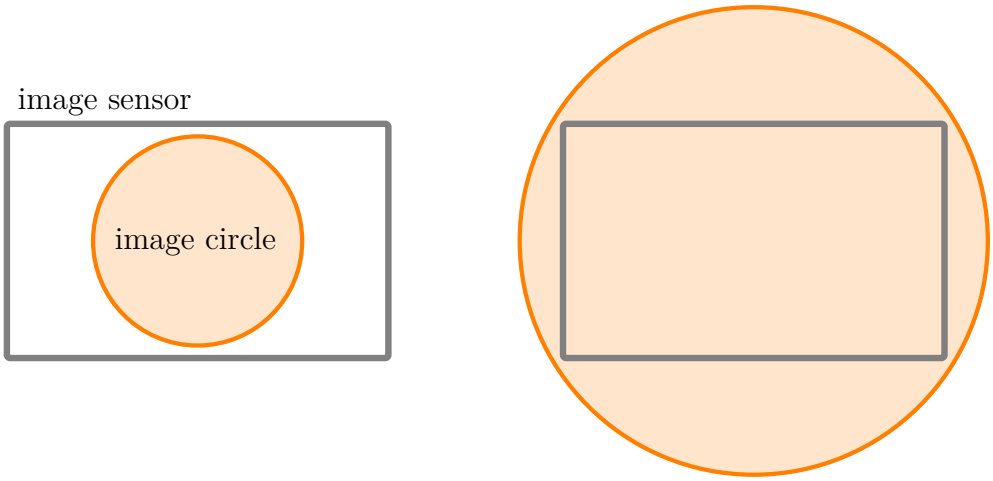

(a) (b)

Figure 9: Examples of (a) circular and (b) full-frame projections.

The four most common lens projection geometries for fisheye cameras are equidistant, equisolid, orthographic, and stereographic [19]. The mapping or projection function of a fisheye lens defines the distorted projection distance as a function of incident angle $r_{\mathrm{d}}(\theta_{\mathrm{oa}})$. The four fisheye mapping functions are visualized in Figure 10 along with the rectilinear mapping function (13) of the pinhole camera model.

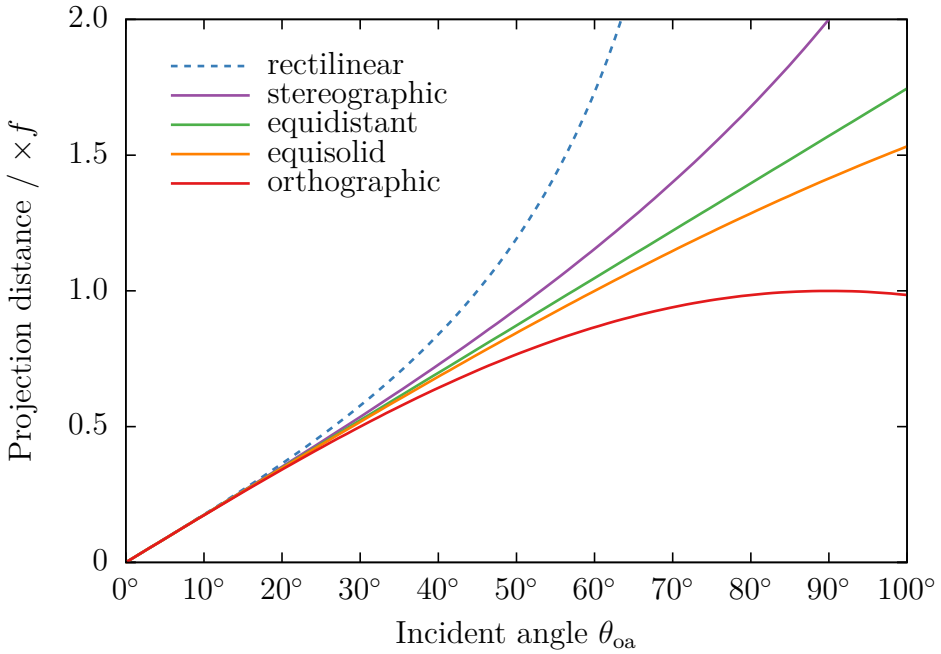

Figure 10: Projection distance r from the image center as a function of incident angle for four fisheye lens geometries and the rectilinear mapping function of the pinhole camera model. The projection distance is shown as the multiples of the focal length f.

At small incident angles θ_{oa}, all the functions in Figure 10 result in a similar projection distance, and thus, similar images in the central regions. As the incident angle grows, the projection distance of the rectilinear mapping function increases drastically. Fields of view of close to 180°, or larger, are practically impossible to accomplish using the rectilinear projection.

Most fisheye lenses are made to comply with the equidistant or equisolid projection functions and less frequently with orthographic or stereographic mapping functions. In equidistant projection, the radial distance r_{d} is directly proportional to the incident angle θ_{oa}

$$r_{\mathrm{d}}(\theta_{\mathrm{oa}}) = f\theta_{\mathrm{oa}}\,. \tag{19}$$

Therefore, lenses conforming to equidistant projection are suitable for measuring angles in radial direction. The equivalent undistorted distance for the equidistant distortion function can be solved from

$$r_{\mathrm{d}}(r_{\mathrm{u}}) = f\tan^{-1}\left(\frac{r_{\mathrm{u}}}{f}\right) \Leftrightarrow r_{\mathrm{u}}(r_{\mathrm{d}}) = f\tan\left(\frac{r_{\mathrm{d}}}{f}\right)\,. \tag{20}$$

The inverse of a distortion function can be utilized to rectify photographs taken with the respective fisheye lens. [19]

The equisolid projection maintains the ratio of an incident solid angle and the resulting image area making it applicable for area measurements. Because of the constant ratio between the incident solid angle and the resulting image area, the mapping function is also called equal-area projection. The mapping function for equisolid projection and the inverse of the distortion function are

$$r_{\mathrm{d}}(\theta_{\mathrm{oa}}) = 2f\sin\left(\frac{\theta_{\mathrm{oa}}}{2}\right) \text{ and} \tag{21}$$

$$r_{\mathrm{u}}(r_{\mathrm{d}}) \;= f\tan\left(2\sin^{-1}\left(\frac{r_{\mathrm{d}}}{2f}\right)\right)\,, \tag{22}$$

respectively. [19]

A lens which conforms the orthographic projection deflects an incoming light ray to be parallel with the optical axis. The orthographic projection function and the inverse of its distortion function are respectively

$$r_{\mathrm{d}}(\theta_{\mathrm{oa}}) = f\sin\left(\theta_{\mathrm{oa}}\right) \text{ and} \tag{23}$$

$$r_{\mathrm{u}}(r_{\mathrm{d}}) \;= \frac{r_{\mathrm{d}}}{\sqrt{1-\dfrac{r_{\mathrm{d}}^2}{f^2}}}\,. \tag{24}$$

The orthographic projection suffers from greater distortions on large incident angles than the other projection geometries. It is also not adequate for systems that require

more than hemispherical field of view because the sensor areas are overlaid twice for the incident angles over 90°, as can be seen in Figure 10. [17]

Stereographic projection preserves angles between objects in the camera coordinate system and the image. The mapping function of the stereographic projection and the inverse of the distortion function are respectively

$$r_{\mathrm{d}}(\theta_{\mathrm{oa}}) = 2f \tan\left(\frac{\theta_{\mathrm{oa}}}{2}\right) \text{ and} \tag{25}$$

$$r_{\mathrm{u}}(r_{\mathrm{d}}) \ = f \tan\left(2 \tan^{-1}\left(\frac{r_{\mathrm{d}}}{2f}\right)\right) . \tag{26}$$

Because the projection maintains angles, also the proportions of the objects are retained.

Typically, lens manufacturers design fisheye lenses to conform with one of the aforementioned projection functions but due to tolerances in manufacturing process additional correction parameters may be required. Besides the mapping functions used to model the projection of the lens, there are several radial lens models which rely on polynomials. Such models are independent of the underlying projection function, and in addition to the designed radial distortion, they can also take into account possible deviations from the ideal mapping function. The parameters for these models require estimation. [17]

4 Developed fisheye camera method

In this chapter, the developed method for spatial non-uniformity corrections in measurements with integrating spheres is described in detail. First, an overview of the method is given. After the overview, the utilized imaging hardware and its geometric calibration method are presented. The measurement procedure is then discussed in detail by going through the phases required to obtain the spatial correction factor. Finally, the developed measurement and analysis software is presented.

4.1 Overview of the method

Essentially, the developed method aims to reconstruct the inner surface of the integrating sphere from an image captured with a fisheye lens camera, and then resolve the relative angular intensity distribution of the lamp from the recorded intensity values of the inner surface of the reconstructed sphere. The measurement equipment consists of a personal computer running the developed measurement software, a fisheye camera, and a camera adapter for the integrating sphere. The equipment is presented in Figure 11.

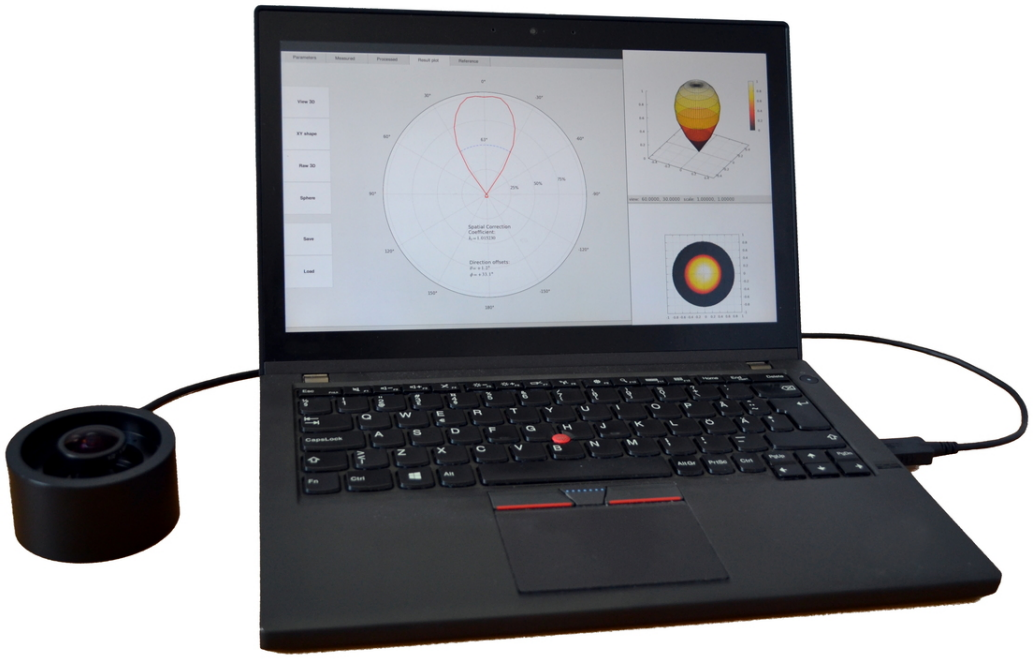

Figure 11: A photograph of the measurement equipment.

Before any measurements, the intrinsic parameters of the imaging hardware must be determined using a geometric camera calibration procedure. This is a one

time procedure for a camera, assuming that its hardware remains intact after the calibration.

The first step in determining the spatial correction factor is imaging of the interior of the integrating sphere illuminated by a light source which is as omnidirectional as possible. The captured image is used to estimate the camera pose and as a reference for the image processing of the following measurement photographs. The reference image and all the following images of the DUTs are taken in a way that reduces the interference caused by the flicker of the lamps.

The second phase is capturing an image of the DUT operated inside the sphere. After imaging the DUT, the photograph is processed to decrease the impact of noise, imaging system imperfections, and the spatial non-uniformity elements of the integrating sphere. The processed image is then used to reconstruct the three dimensional sphere model.

From the reconstruction, the relative angular intensity distribution $I_{\mathrm{v}}(\theta_{\mathrm{DUT}}, \phi_{\mathrm{DUT}})$ of the lamp and the location of the center of the radiation pattern are determined. The results are combined to obtain the relative angular intensity distribution $I_{\mathrm{v}}(\theta, \phi)$ inside the sphere to calculate the spatial non-uniformity correction k_{s} according to equation (7).

4.2 Imaging hardware

The imaging hardware was chosen to comply with the size requirement set by the detector port of the integrating sphere at the MRI. The 23.3 mm inner diameter of the port, and the intent to keep the sphere unmodified, limited the selection to small camera modules. Photographs of the two cameras chosen for the work are shown in Figure 12.

(a) (b)

Figure 12: Photographs of (a) Camera 1 and (b) Camera 2 installed into the adapter for the integrating sphere at the MRI.

Camera 1 is an inexpensive universal serial bus (USB) camera module that uses the generic camera driver interface provided by the operating system [20]. A 180° field of view fisheye lens is supplied with the module. The diameter of the image circle created by the equisolid lens is larger than the vertical dimension of the complementary metal-oxide-semiconductor (CMOS) image sensor, resulting in reduced field of view in the vertical direction.

Camera 2 is an industrial grade USB camera module with a separate fisheye lens [21, 22]. The camera requires the manufacturer's proprietary driver software to operate. The diameter of the aperture of the detector port constrained the selection of the lens. As a result, the field of view of the camera is wider than 180° which results in some image data from the inside of the detector port to be projected on the CMOS sensor as well. The lens for Camera 2 is also designed to conform with the equisolid mapping function.

Both cameras have fixed apertures and focal lengths. Default gain values for individual color channels were used throughout the measurements. The key characteristics of both cameras are presented in Table 2.

Table 2: Technical specifications of the cameras

Feature	Camera 1	Camera 2
Image sensor type	CMOS color	CMOS color
Sensor size (µm)	5856 × 3276	7200 × 5400
Pixel resolution	1920 × 1080	1600 × 1200
ADC resolution	10 bit	10 bit
Lens FOV	180°	185°
Projection function	equisolid	equisolid
Produced image	nearly circular	circular

Ten bit resolution of analog-to-digital converter (ADC) of both cameras corresponds to the theoretical maximum of 1024 intensity levels of the relative angular intensity distribution for each DUT. In practice, because of the diffuse reflected light inside the sphere, the effective ADC resolution is significantly lower and depends on the beam angle and the absolute luminous intensity of the angular distribution of the DUT. The diffuse reflected light is the main component limiting the signal-to-noise ratio (SNR) of the fisheye camera measurement for the relative angular intensity distribution of the DUT.

To mount the cameras into the detector port of the integrating sphere at the MRI, an adapter was designed (shown in Figure 12). The adapter was designed in such a way that it could be used for both cameras. The part was machined from polyoxymethylene (POM) thermoplastic which is a material of high stiffness and dimensional stability [23]. The mechanical design drawing of the adapter is presented in Appendix A.

4.3 Geometric camera calibration

In addition to the technical specifications provided by the camera and lens manufacturers, the intrinsic camera parameters $\boldsymbol{K}$ of equation (16) need to be estimated to account for the imperfections of the hardware. These mechanical nonidealities are caused by the internal misalignment of the camera assembly [24] and thus, the intrinsic parameters will vary even between different units of the same camera model.

Estimation of camera parameters is also known as geometric camera calibration. The calibration relies on the knowledge about the correspondences between a calibration target with a known composition and one or more photographs of the target [25, 26]. The calibration target is often chosen to contain corners, dots, or some other features that can be easily identified [11]. The intrinsic parameters of both cameras were calibrated using a camera calibration toolbox for Matlab [27].

The printed checkerboard pattern used for the calibration is shown in Figure 13. The original fisheye photograph in Figure 13 (a) is rectified to correspond to the undistorted view. The grainy right and left sides in (b) are the result of scarcer data as the incident angle grows. Despite approximately the same image area, the rectified image lacks the information from the peripheries of the fisheye image.

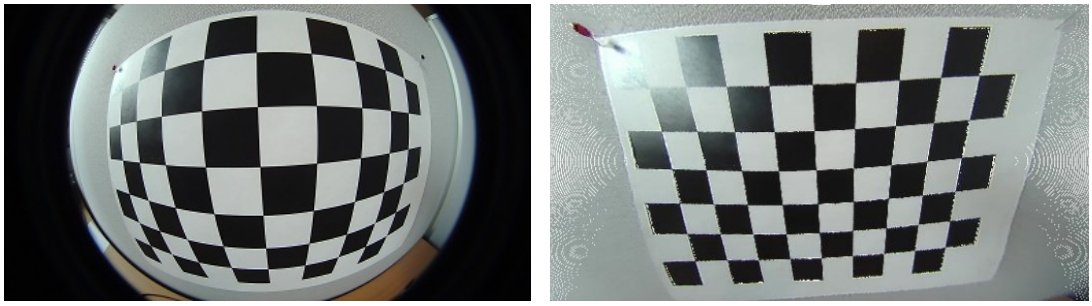

(a) (b)

Figure 13: (a) A photograph of the calibration pattern. (b) Rectification of (a) using the estimated intrinsic parameters and the equisolid inverse function.

The utilized calibration tool requires a minimum of three images of the calibration pattern as an input, but at least ten is recommended. The routine automatically detects the corners of the checkerboard in the provided images and outputs the intrinsic parameters $\boldsymbol{K}$. It also solves the extrinsic parameters $\boldsymbol{R}$ and $\boldsymbol{t}$ for each calibration image.

4.4 Measurement procedure

4.4.1 Imaging the integrating sphere

To image the inner surface of the sphere, the camera is installed into the adapter and mounted into the detector port of the sphere. Before measuring any DUTs,

a reference image is taken with the sphere illuminated by a bulb type lamp with angular intensity distribution as uniform as possible. A reference image captured with Camera 1 is shown in Figure 14 along with a ray tracing image using a mathematical camera model with an equisolid fisheye lens and intrinsic parameters of Camera 1. The integrating sphere model shown in Figure 2 was used for the simulated image. The model was illuminated by an ideal isotropic light source at the center of the sphere. The model and the simulation was done using Cycles ray tracing render engine of open source rendering software Blender [28].

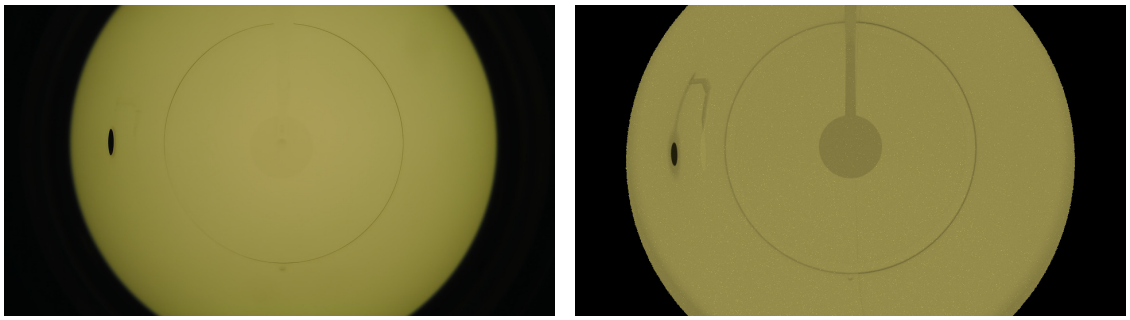

(a) (b)

Figure 14: (a) A reference image taken through the detector port of the integrating sphere using Camera 1. (b) A simulated reference image using equivalent camera parameters: lens projection function, camera pose, and intrinsic parameters.

By comparing the two reference images in Figure 14, it can be seen that the real world camera exhibits noticeable light fall-off towards the peripheries of the image circle. The fall-off on the edges caused by the camera optics is particularly common in systems with non-full-frame projections [29]. The optical axis of the camera is also inclined downwards. The captured reference image is used for taking into account the darkening in the image caused by the imaging hardware and the spatial luminous responsivity of the sphere. The process is described in Section 4.4.3.

Most measured AC-operated SSLs produce considerable flicker which affects the images. Camera 1 has a rolling shutter which scans the image sensor one pixel row at a time when capturing a single frame. This causes the captured image to have darker and brighter horizontal regions. Camera 2 has a global shutter which captures the entire frame at the same instant, thus the flicker is seen as a pulsing intensity level of the whole frame. The impact of the effect is reduced by capturing and averaging multiple images. The images are captured over a period of several PLCs with a variable frame rate. Aside from flicker, averaging multiple photographs reduces random noise in the final image. A number of frames used to calculate the averaged image depends on the DUT and the camera; cameras with a rolling shutter require more photographs to even out the image.

The intensity values of the areas of interest of the captured images must remain

within the dynamic range of the camera. For the areas illuminated directly by the DUTs, utilization of the dynamic range should also be maximized. Thus, the exposure time must be as long as possible without overexposing any color channels of any pixels. Because of flicker, finding the sufficient exposure time is an iterative process of reducing the exposure time until none of the captured frames have overexposed pixels.

4.4.2 Camera pose estimation

In order to resolve the angular intensity distribution of the DUT from a photograph, the extrinsic camera parameters need to be estimated. The location of the center of projection of the camera is assumed to be at $(r, \theta, \phi) = (R_\mathrm{s},\, 90°,\, 180°)$ as shown in Figure 6. The location corresponds to the translation vector $\boldsymbol{t} = \begin{pmatrix} 0 & -R_\mathrm{s} & 0 \end{pmatrix}^\mathrm{T}$. In contrast to the translation, the rotation of the camera may deviate considerably from the orthogonal geometry. Since the rotation inside the detector port can only be controlled about one axis, the other two are determined by the mechanical properties of the port and the camera assembly.

To obtain the camera pose, at least two point features of known locations need to be detected from the reference image. The optimal choice of these features depends on the integrating sphere. The sphere at the MRI is equipped with a prominent external port, and the center of the sphere can be robustly detected. The sphere center is found using the Hough transform, which is a feature extraction method used to detect shapes that can be specified in a parametric form [30]. In the case of the sphere center, it is sufficient to find the circle formed by the seam structure between the two hemispheres. The sphere center lies on the line between the principal point and the center of the circle at a distance R_s from the center of projection. As can be seen in Figure 10, for deviation angles under 5°, the radial lens distortion is negligible; a maximum of 0.3 % at 5.0° for equisolid projection. Thus, the camera pose can usually be estimated directly from a distorted image.

In the reference image taken of the integrating sphere at the MRI (Figure 14), the external port is the most prominent dark blob. Such a feature can be detected by converting the photograph to a binary image using a low threshold and finding the center of the intensity minimum. Dark areas outside the image circle are filtered out based on the size of the area. For the purpose of resolving the camera pose, accurately detecting the external port center in the radial direction is not critical.

An image with the detected sphere center, external port, and the lines indicating the rotation of the camera is presented in Figure 15. The white dot lies in the center of the circle and represents the detected center of the sphere. The red dot is the image center and the short straight line between the two points indicates the pitch and yaw of the camera. The long straight line between the sphere center and the external port indicates the roll of the camera.

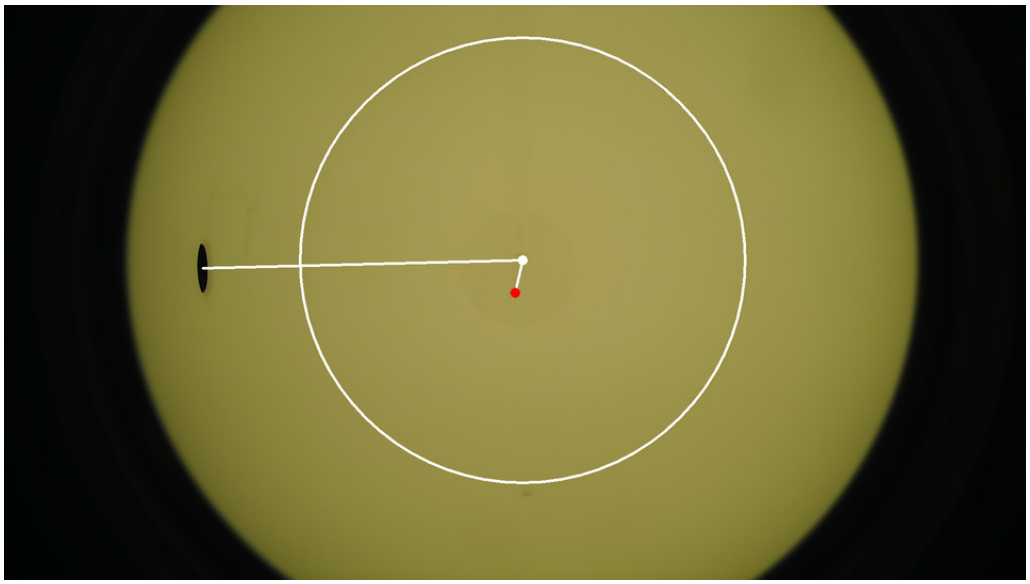

Figure 15: An image of the inner surface of the sphere with the detected features for resolving the camera pose. The white and red dots are the detected sphere center and the principal point, respectively.

From the obtained locations of point features, intrinsic parameters of the camera, and the assumption of the translation vector $\boldsymbol{t} = \begin{pmatrix} 0 & -R_\mathrm{s} & 0 \end{pmatrix}^\mathrm{T}$, using right angle trigonometry, it is possible to calculate the pitch α_c, yaw β_c, and roll γ_c angles of the camera with respect to the orthogonal camera coordinate system.

The rotation matrix which describes the orthogonal geometry in Figure 6 is respectively adjusted to reflect the resolved angles. The adjusted rotation matrix is obtained according to [31]

$$\boldsymbol{R} = \begin{bmatrix} \cos\gamma_\mathrm{c} & -\sin\gamma_\mathrm{c} & 0 \\ \sin\gamma_\mathrm{c} & \cos\gamma_\mathrm{c} & 0 \\ 0 & 0 & 1 \end{bmatrix} \begin{bmatrix} \cos\beta_\mathrm{c} & 0 & \sin\beta_\mathrm{c} \\ 0 & 1 & 0 \\ -\sin\beta_\mathrm{c} & 0 & \cos\beta_\mathrm{c} \end{bmatrix} \begin{bmatrix} 1 & 0 & 0 \\ 0 & \cos\alpha_\mathrm{c} & -\sin\alpha_\mathrm{c} \\ 0 & \sin\alpha_\mathrm{c} & \cos\alpha_\mathrm{c} \end{bmatrix} \boldsymbol{R}_\mathrm{o}\,, \tag{27}$$

where $\boldsymbol{R}_o$ is the rotation matrix for the orthogonal geometry in equation (9).

4.4.3 Image processing

The goal of image processing, performed on an image taken of the inner surface of the integrating sphere with a DUT, is to bring out the features of the angular intensity distribution of the DUT and to diminish the impact of the spatial non-uniformity of the sphere. To obtain intensity values of each image pixel, the red, green, and blue (RGB) color channels are combined into a single channel producing a grayscale image. The RGB channels are weighted using coefficients that are meant to preserve

the luminance of the color according to

$$\boldsymbol{Y} = 0.299 \times \boldsymbol{R}_{\text{ch}} + 0.587 \times \boldsymbol{G}_{\text{ch}} + 0.114 \times \boldsymbol{B}_{\text{ch}}\,, \tag{28}$$

where $\boldsymbol{Y}$ is the resulting two dimensional matrix, whose elements are the luminous intensity values of the pixels of the color image [32].

The grayscale image is filtered to remove noise, smooth out the beam pattern, and blur the structural features of the sphere, such as the seam and the lamp holder at the bottom of the sphere. The filtering is done by convolving the image with a discrete Gaussian smoothing kernel, which effectively diminishes high frequency components of the image. An illustration of a continuous Gaussian spatial filter is presented in Figure 16. The x and y axes of the filter are parallel to the respective axes of the image plane coordinate system.

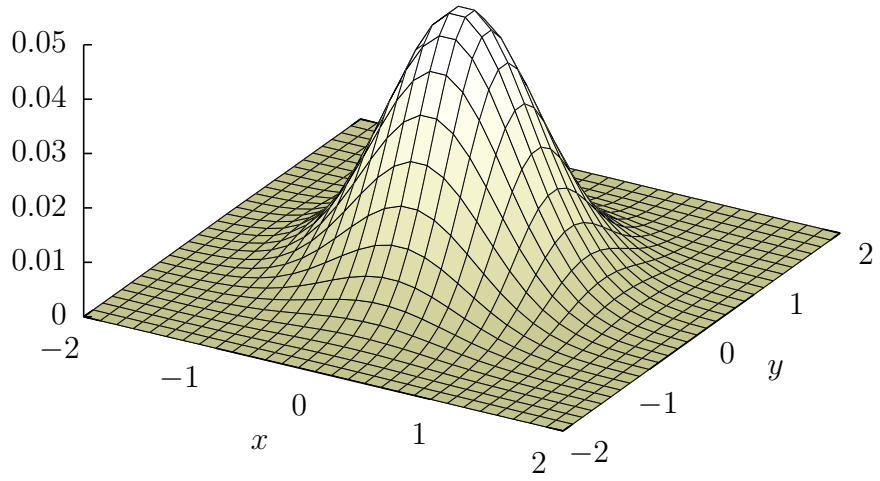

Figure 16: A spatial low pass filter.

To eliminate the external port and the areas close to and outside the border of the image circle, a mask is created from the reference image, which is also filtered using a Gaussian smoothing matrix. To create the mask, the areas with low intensity values are filtered out by thresholding the image. The mask matrix is then normalized and all its elements are replaced with the respective reciprocals. The resulting mask and the filtered intensity matrix $\boldsymbol{Y}$ are then multiplied element-wise. Ultimately, this operation aims to even out the intensity values of the areas which are not illuminated by the direct luminous flux of the DUT. The operation applies a correction, which compensates for the uneven spatial responsivity of the imaging hardware and takes into account the spatial non-uniformity of the sphere, by giving greater gain values for regions that were darker in the reference image. Essentially, this is equivalent to a

flat-field correction used in digital imaging [33], but applied to the whole system. A measurement image of a spot type LED lamp and the result of the image processing is presented in Figure 17.

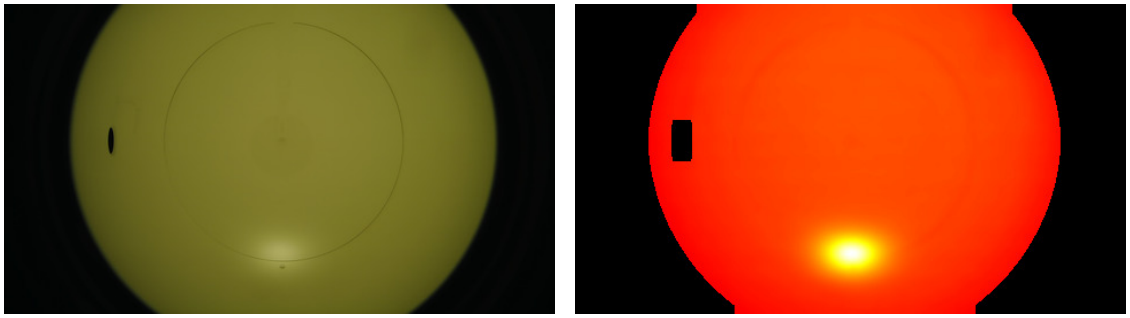

(a) (b)

Figure 17: (a) An image of the integrating sphere with a spot type DUT which has a concentrated angular intensity distribution. (b) The result of the image processing routine. The processed grayscale image is visualized with a colormap.

The structural features of the integrating sphere in the processed image in Figure 17 (b) are less distinguishable than in the original measurement photograph. Most importantly, the image processing routine has reduced the impact of the seam of the integrating sphere on the directly illuminated area on the bottom of the sphere. In addition, the combination of the spatial filtering and the image mask has eliminated areas close the peripheries of the dark regions.

4.4.4 Reconstruction of the sphere from an image

Viewing an object from the side introduces perspective foreshortening in addition to the lens distortion. Because of this, a mere rectification of the fisheye image is not sufficient. To be able to accurately tell the shape and size of the radiation pattern on the bottom of the sphere, it is advantageous to be able to look at it from the center of the sphere.

To reconstruct the three dimensional scene from a photograph, the geometric image formation theory, introduced in the previous chapter, is applied in the reverse order. Besides an image, additional information must be provided to make up for the lost depth data in the photograph. In the case of the integrating sphere, the depth data for each image point can be calculated from the distance of the detector port to the sphere wall in the direction of the original incident angle.

The mapping from the pixel coordinates of a point p_i to the angle of the original incident light ray $(\theta_\mathrm{oa}, \phi_\mathrm{oa})$ of the respective world point ${}^\mathrm{w}\boldsymbol{P}$ is obtained by first calculating the image plane coordinates of the pixel by solving equations (14) and (15) for x and y. This gives the distorted distance r_d of the pixel to the principal point. By

applying the inverse of the distortion function of the lens, the distance is undistorted. This allows using the pinhole camera model equation (13) to solve the incident angle θ_{oa}. The respective angle ϕ_{oa} can be solved from the ratio of x and y.

The angle data is combined with the information about the distance to the sphere wall to get the camera coordinate system point ${}^{\mathrm{C}}\boldsymbol{P} = \begin{pmatrix} X & Y & Z \end{pmatrix}^{\mathrm{T}}$. Finally, from equation (10), it is possible to solve the world coordinate system point

$$\begin{pmatrix} {}^{\mathrm{W}}\boldsymbol{P} \\ 1 \end{pmatrix} = \boldsymbol{T}^{-1} \begin{pmatrix} {}^{\mathrm{C}}\boldsymbol{P} \\ 1 \end{pmatrix}, \tag{29}$$

where $\boldsymbol{T}^{-1}$ is the inverse of the transformation matrix $\boldsymbol{T}$. The process is executed for every image pixel. A sphere, reconstructed from the processed measurement image in Figure 17 (b), is presented in Figure 18.

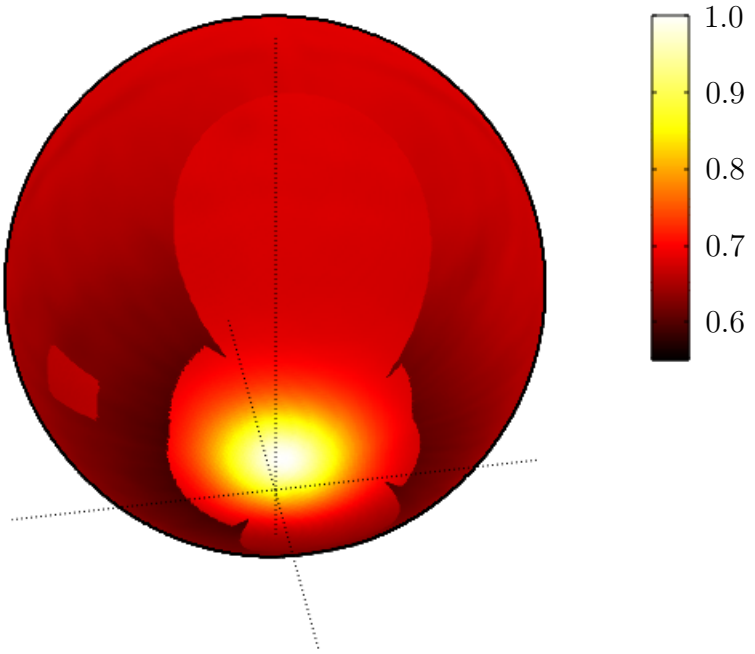

Figure 18: Reconstruction of the integrating sphere using the images in Figure 17 as viewed from $\{\theta = 50°, \phi = 170°\}$. The lines intersect at the sphere bottom $\theta = 180°$.

The holes in the sphere in Figure 18 are caused by missing and filtered out data. The external port and the area in the vicinity of the detector port are filtered out due to their low intensity values. The two larger areas above and below the general area of the detector port are missing because the image circle diameter is larger than the vertical sensor length (see Figure 9). The upper missing area is larger as a result of the camera pose; the optical axis of the camera is inclined downwards. As can be seen in Figure 18, the central beam does not coincide with the bottom of the sphere

due to the inclined lamp holder and a possible mismatch between the mechanical and optical axes of the SSL.

4.4.5 Resolving the relative intensity distribution

In addition to the high intensity values of the points exposed to the direct luminous flux from the DUT, diffuse reflected light causes other points of the sphere surface to be illuminated as well. This ambient illumination is estimated by the mean of the intensity values of the hemisphere on the opposite side from the points directly illuminated by the central beam of the lamp. For most measured SSLs, the heading direction of the central beam can be resolved by finding the intensity maximum of the reconstructed sphere.

The obtained ambient illumination is subtracted from the intensity values of all points of the reconstructed sphere. The intensity values are normalized after the subtraction. The reconstructed sphere without the ambient light is shown in Figure 19.

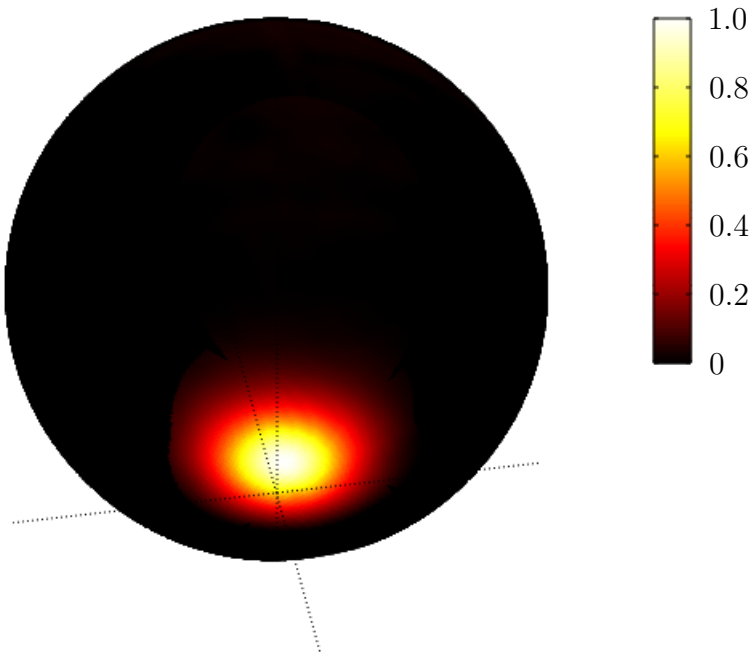

Figure 19: The reconstructed sphere model with eliminated diffuse illuminance, as viewed from the direction $\{\theta = 50°, \phi = 170°\}$.

By replotting the data used in Figure 19 so that the distance of each point of from the world coordinate system origin is determined by the normalized intensity value of the point, it is possible to obtain the three dimensional radiation pattern of the DUT. The unprocessed radiation pattern of the lamp of the reconstructed sphere in Figure 19 is presented in Figure 20.

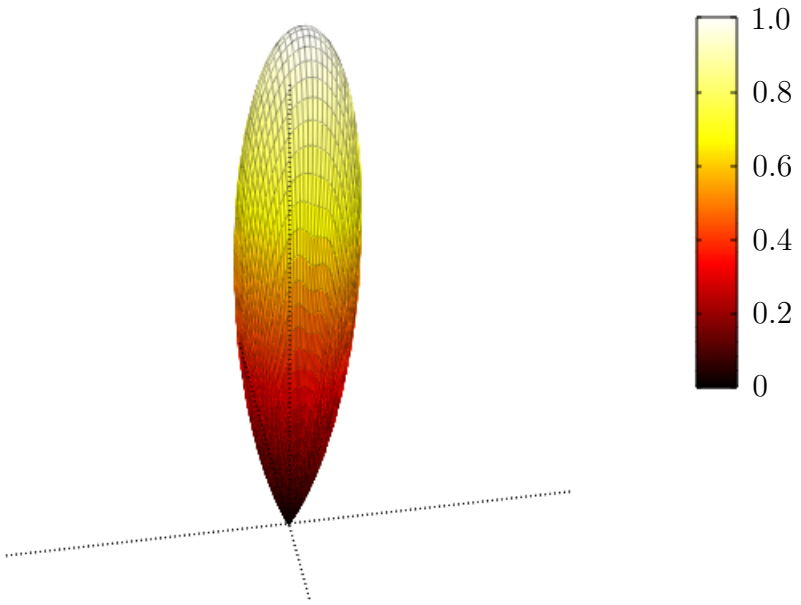

Figure 20: The data used to plot the sphere illuminated by a DUT in Figure 19 with the distance to the origin determined by the intensity value of each point. The z axis of the world coordinate system is inverted for the illustration purposes.

The relative angular intensity distribution $I_{\mathrm{v}}(\theta_{\mathrm{DUT}}, \phi_{\mathrm{DUT}})$ can be resolved from the determined offset between the negative z axis and the central beam, and solving the intensity values for all $(\theta_{\mathrm{DUT}}, \phi_{\mathrm{DUT}})$ at the required resolution. Because of the unpredictable ϕ_{DUT} angle, when using a E27-base lamp holder, and the rotational symmetry of the radiation pattern about the optical axis of the lamp, the intensity values of each θ_{DUT} step are averaged over ϕ_{DUT} angles. This also aids to reduce the effect of spatial non-uniformities of the integrating sphere; especially when measuring lamps with wide beam angles.

4.5 Software for automated measurements

To automate the described measurement procedure and the calculation of the respective spatial correction factor k_s, a piece of software was developed. The program was written using Python programming language in compliance with Python Enhancement Proposal 8 (PEP 8) – *Style Guide for Python Code* [34]. The program is composed of a back-end layer which provides the functionality to one of the two alternative front-ends: the command line interface (CLI) and the graphical user interface (GUI).

The back-end layer is based on the scientific computing package NumPy [35] and the computer vision library OpenCV [36]. OpenCV is used as the interface for the imaging hardware, image processing, and feature detection. It also provides visual output of the measurement results for the CLI. The sphere reconstruction, including all geometric transformations, and calculation of relative angular intensity

distributions and the respective correction factors is implemented using mathematical functions provided by NumPy.

The GUI of the developed software is presented in Figure 21. Both front-ends provide means to capture the reference and DUT measurement images, perform image processing, and carry out the subsequent calculations to finally obtain the spatial correction factor using an existing SRDF file. The calculated data is saved along with the captured images.

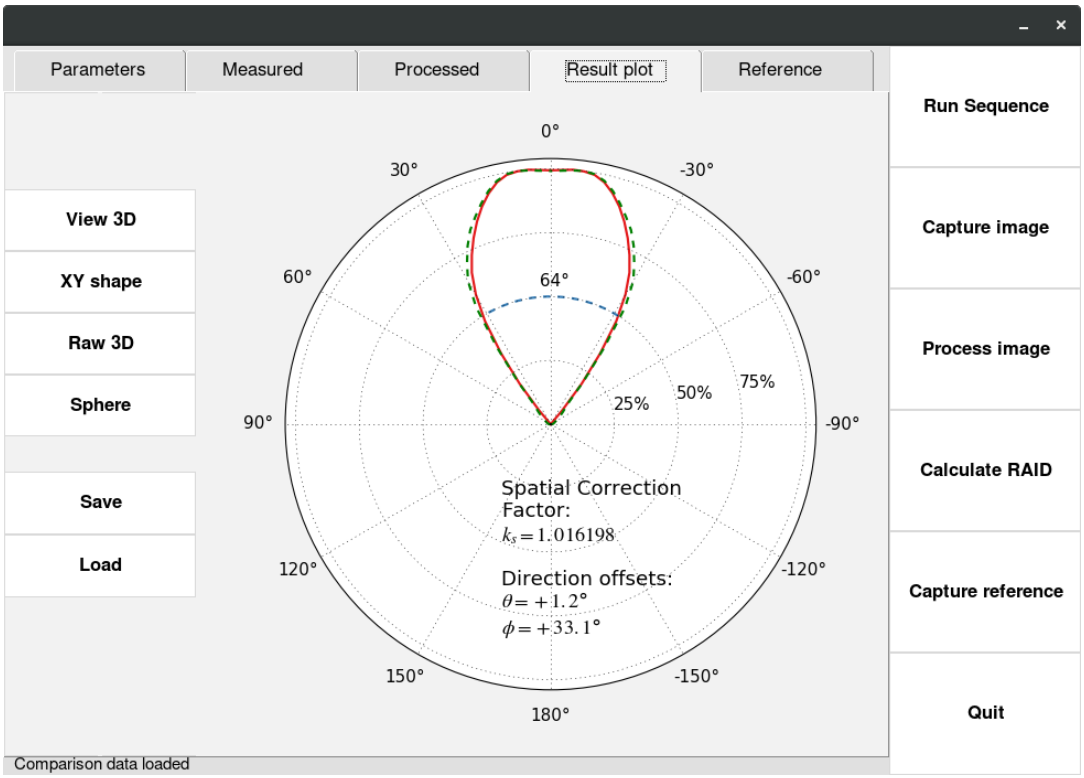

Figure 21: The graphical user interface of the developed software for determining spatial non-uniformity corrections.

In addition to the aforementioned features, the GUI assists in camera alignment, supports loading intrinsic parameter files for different cameras, and allows to manually override the detected camera pose and the DUT pointing direction offsets. Using the GUI, it is also possible to load previously measured data for comparison. In Figure 21, the reference angular data of the SSL measured using the goniophotometer are displayed using the green dashed line.

5 Validation results

In this chapter, the results of the validation measurements of the fisheye camera method are presented. The relative angular intensity distributions of twelve SSLs obtained using the fisheye camera method and the goniophotometer used as a reference are compared. Also, the impact of the deviations in intensity distributions on the spatial non-uniformity correction factor is studied. The chapter is concluded with the uncertainty analysis of the developed method.

5.1 Validation measurements

To validate the functionality of the developed fisheye camera method, relative angular intensity distributions of twelve SSLs were measured using the two fisheye cameras and the goniophotometer at the MRI (see Figure 5). The results of the goniometric measurements were used as a reference for the fisheye camera method.

For the reference image of the fisheye camera method, the integrating sphere was illuminated with a bulb type LED lamp, whose angular intensity distribution is show in Figure 22. The lamp has a beam angle of over 240° and the luminous intensity values within 9 % from the maximum value for $\theta_{\mathrm{DUT}} \leq 60°$. To study the impact of non-uniform intensity distribution of the reference lamp on DUTs with prominent luminous intensity on angles of $\theta_{\mathrm{DUT}} > 60°$, the DUTs were measured using alternative light sources as reference lamps.

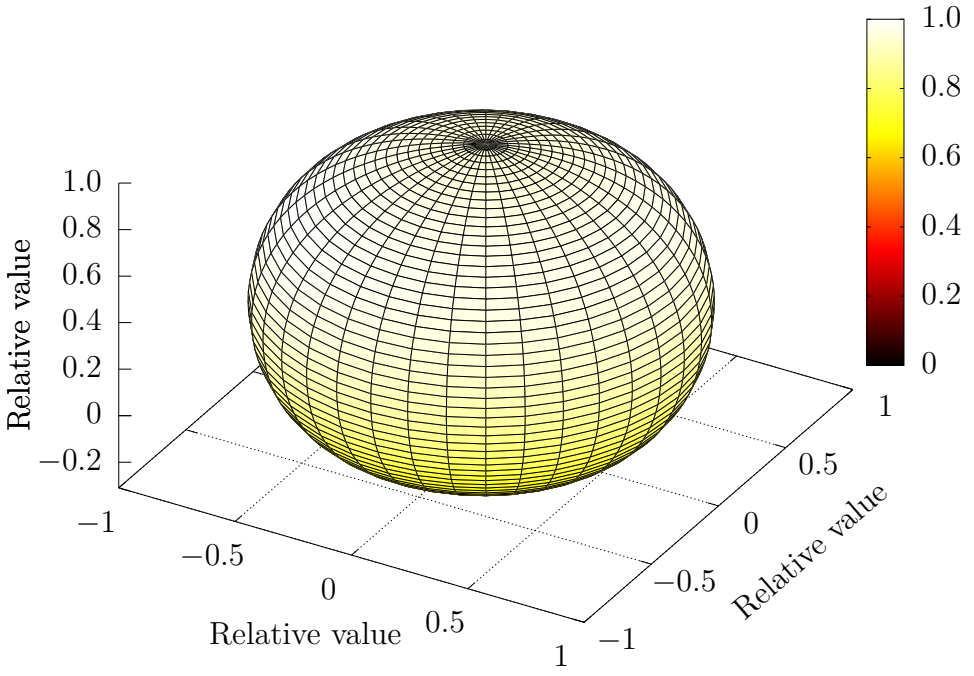

Figure 22: The relative angular intensity distribution of the bulb type lamp used for capturing the reference images for the validation measurements of the fisheye camera method.

All the SSLs were aged for a minimum of three days before the measurements. Ahead of measuring each SSL with the goniophotometer, every DUT was operated for a time period of one hour to stabilize the luminous flux of the SSL. For both methods, the measurement resolution of ($\Delta\theta_{\mathrm{DUT}} = 2.5°, \Delta\phi_{\mathrm{DUT}} = 10.0°$) was used and the obtained intensity distributions averaged for each θ_{DUT} about the optical axis. For the fisheye camera method, no additional stabilization time was employed due to the brief measurement procedure and simultaneous recording of data for all angles.

For all the measurements, the electrical power required by the DUTs was generated using a programmable AC voltage source to ensure the stability of the luminous flux of the SSL during the measurement. The long term stability of the power and flux is particularly important for goniometric angular intensity measurements because of the longevity of the procedure; approximately six hours in these measurements.

5.2 Relative angular intensity distributions

In Figure 23 the relative angular intensity distribution of an SSL measured using the fisheye camera method and the goniophotometer is presented. The distance of each data point to the origin is determined by its luminous intensity value. The data processing steps leading to the resolved distribution are shown in Figures 17–20. The intensity distribution data is scaled into the range $[0, 1]$.

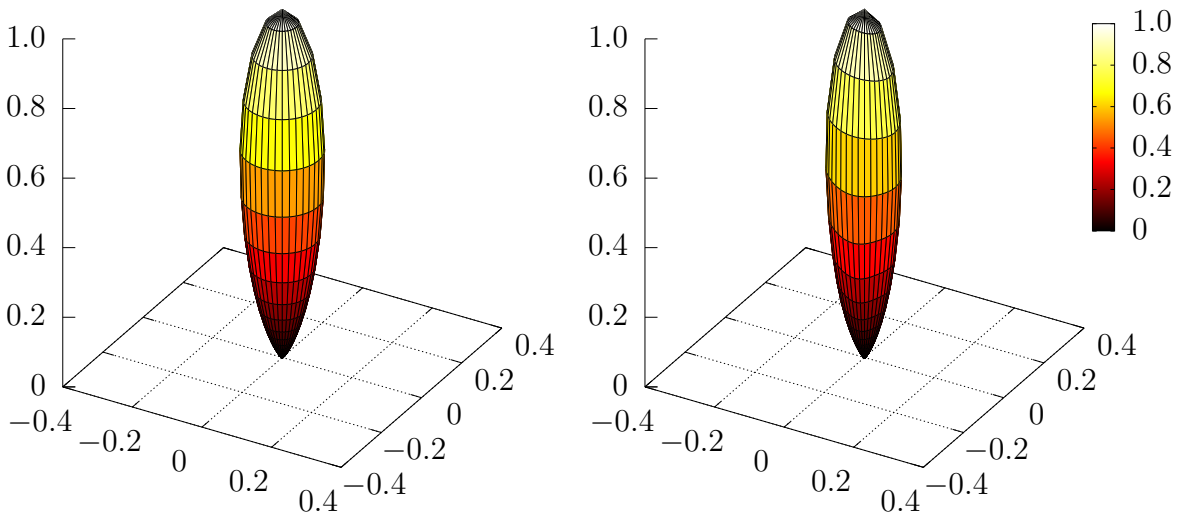

(a) (b)

Figure 23: The relative angular intensity distribution of SSL 1 obtained using (a) the fisheye camera method and (b) the goniophotometer at the MRI. All the axis tick labels are relative values.

SSL 1 in Figure 23 has a concentrated angular intensity distribution. Resolving intensity distributions of lamps with small beam angles requires relatively small $\Delta\theta_{\mathrm{DUT}}$ steps when using a goniometer, which leads to prolonged measurements. On the other hand, when using the fisheye camera method, the difference in intensity levels between the areas exposed to the direct luminous flux and the areas illuminated by the diffuse reflected light is more distinctive when measuring DUTs with small beam angles.

To quantify the difference between the measured relative intensity distributions obtained using the two methods, the weighted mean absolute difference was calculated for the measurement data. The map of absolute differences between the corresponding data points of the intensity distributions of SSL 1 are presented in Figure 24.

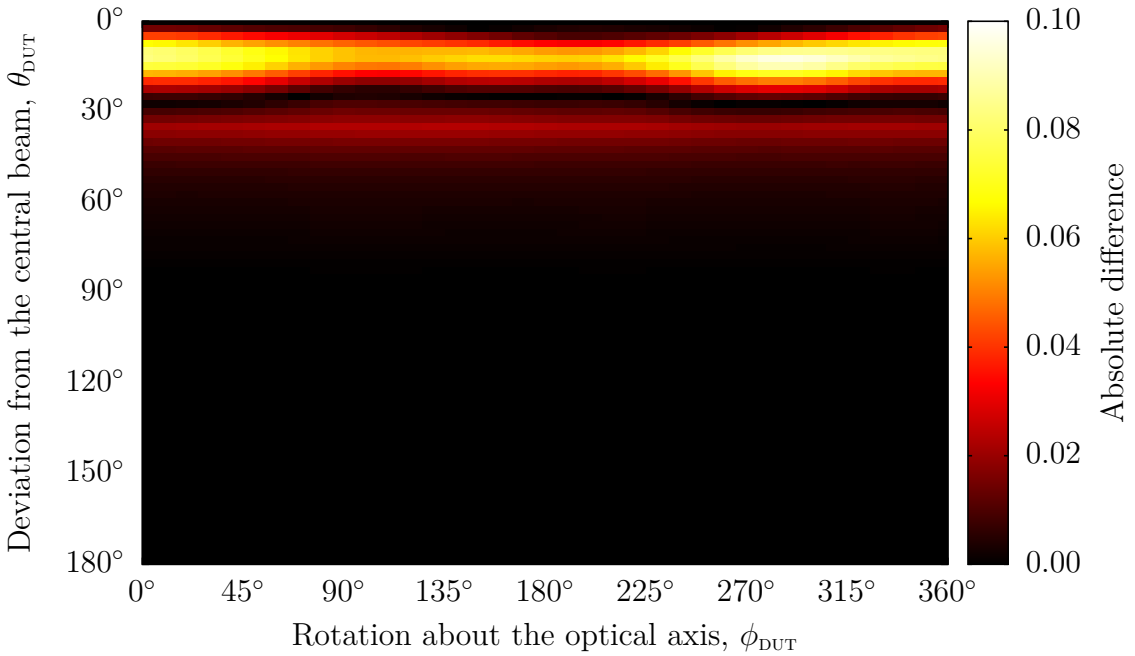

Figure 24: The absolute difference between the normalized relative angular intensity distributions of SSL 1 obtained using the fisheye camera method and the goniophotometer.

By weighting the difference data in Figure 24 by $\sin(\theta_{\mathrm{DUT}})$ due to the spherical coordinates used in the measurements and calculating the mean of the map points, the mean absolute difference is obtained. This value can be used to compare the magnitude of deviations in the relative angular intensity distributions obtained using the two cameras to the goniophotometer reference. The mean absolute differences between the methods for both cameras and the twelve measured SSLs are presented in Table 3. The beam angle of each SSL, calculated from the reference data, is given to coarsely characterize the DUT. The mean absolute difference ($\times 100$) of the angular intensity distributions of an isotropic light source and a complete darkness

would be approximately 63.

Table 3: The mean absolute differences of the relative angular intensity distributions obtained using the fisheye camera method and the reference goniophotometer

DUT	Beam angle	Camera 1 ×100	Camera 2 ×100
SSL 1	21.0°	0.27	0.21
SSL 2	21.0°	0.51	0.43
SSL 3	21.5°	0.27	0.26
SSL 4	28.6°	0.43	0.42
SSL 5	31.4°	0.31	0.37
SSL 6	51.9°	0.88	0.47
SSL 7	55.5°	1.31	1.21
SSL 8	65.1°	1.56	0.82
SSL 9	65.4°	1.36	1.03
SSL 10	80.6°	2.54	2.41
SSL 11	105.4°	6.59	5.58
SSL 12	139.0°	10.70	8.02

From Table 3, it can be seen that there is a correlation between the beam angle and the mean absolute difference value between the methods. Aside from the few exceptions, the relative angular intensity distributions of the lamps with narrower beam angles are closer to their respective goniometrically measured reference than the ones with the wider beam angles.

Both cameras are almost equally capable to resolve the angular intensity distributions of SSLs with concentrated radiation patterns. On larger beam angles, Camera 2 is closer to the goniophotometer reference then Camera 1. The relatively large differences in results between the cameras for high-flicker lamps SSL 11 and SSL 12 are caused by the fact that Camera 2 is less susceptible to flicker due to its global shutter.

Even though the reference light source used for the reference image was not isotropic, the angular intensity distributions of the SSLs 1–5 are almost completely within the uniform region of the reference source. SSL 11 and SSL 12 have substantial intensity levels at the angles of $\theta_{\mathrm{DUT}} > 60°$. By using a reference source with a broader angular distribution, the mean absolute differences (×100) of SSL 11 and SSL 12 reduced to 1.05 and 4.86 for Camera 2 respectively. The effect of changing the reference light source on the relative angular distribution of SSL 11 is visualized in Figure 25.

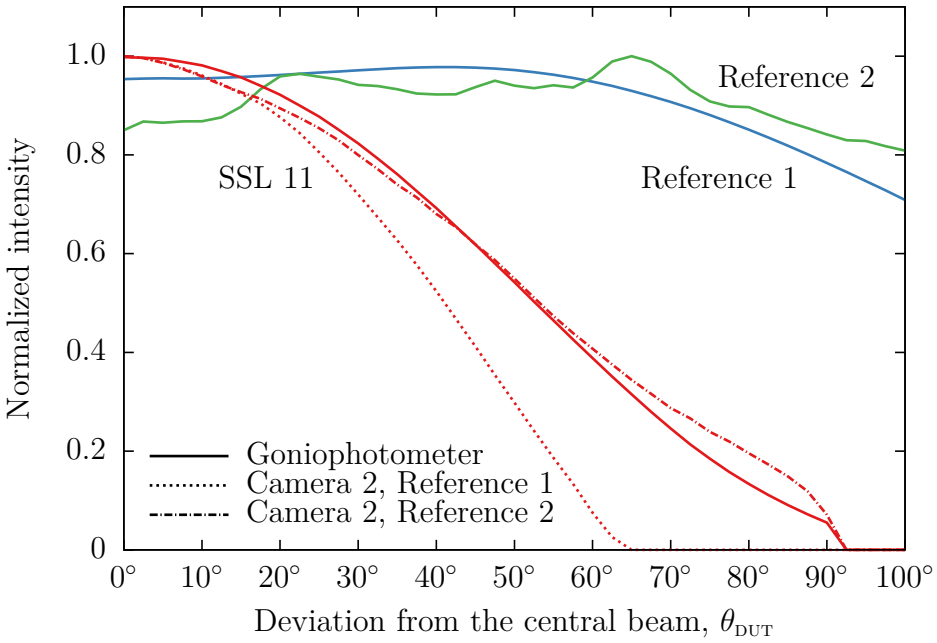

Figure 25: The impact of changing the reference light source for SSL 11 and angular intensity distributions of both reference lamps.

As can be seen in Figure 25, the angular intensity of the original reference source (Reference lamp 1) is within 0.9–1.0 range for the 0° to 60° deviations from the central beam. This results in a relatively uniform reference for the lamps with concentrated radiation patterns. However, for DUTs such as SSL 11, the intensity fall-off at large angles leads to over-conservative estimation of the relative angular intensity distribution of the DUT. On the other hand, the uneven angular distribution of the alternative reference light source (Reference lamp 2) leads to the mean absolute difference ($\times 100$) of 0.83 for SSL 1.

Aside from assigning too small gain values for the intensities of the pixels on large θ_{DUT} angles, the reference light fall-off leads to an overestimation of the diffuse illumination inside the integrating sphere. This consequently leads to erroneous background signal removal for all the pixels and results in obtaining too narrow angular intensity distribution for the DUT.

While the results of the goniometric measurements are assumed to be the point of reference, the goniophotometer at the MRI is sensitive to the mechanical imperfections of the measured SSLs. A lamp with a skewed base is particularly problematic, since it is impossible to compensate for the misaligned optical axis in advance. In turn, the fisheye camera method is unsusceptible to deviations between the optical and mechanical axes of a DUT. Out of the measured lamps, SSL 7 has a noticeably skewed base. In Figure 26, the relative angular intensity distribution of SSL 7 obtained using Camera 2 and the goniophotometer is shown. The effect of the skewness of the distribution obtained with the goniophotometer is noticeable in the mean absolute deviation of SSL 7 in Table 3.

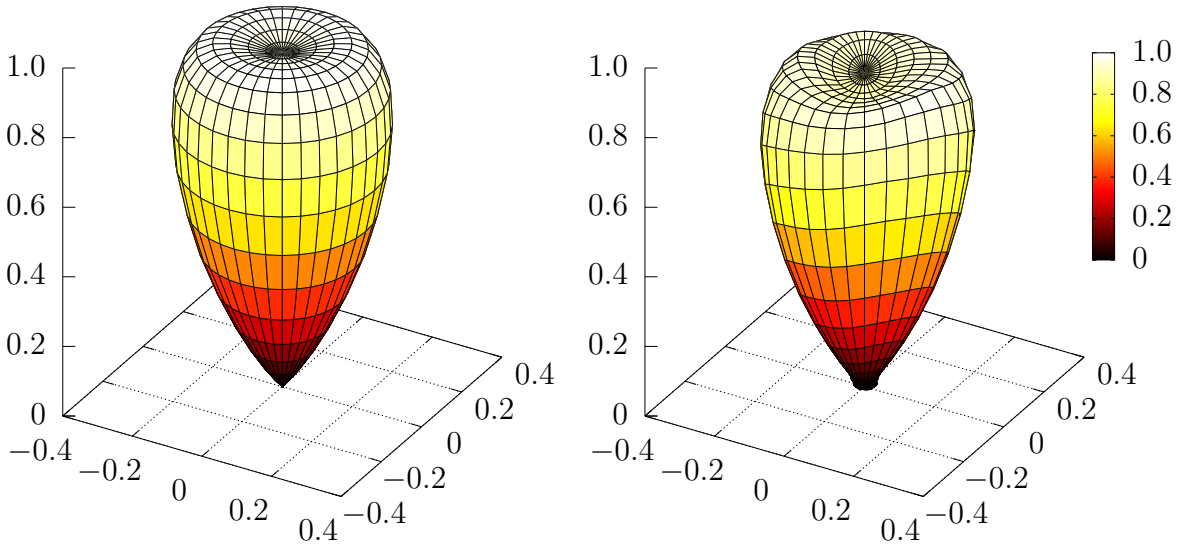

(a) (b)

Figure 26: Comparison of the relative angular intensity distributions of SSL 7 obtained using (a) the fisheye camera method and (b) the goniophotometer. All the axis tick labels are relative values.

For the rotationally asymmetrical angular intensity distribution of SSL 7 in Figure 26 (b), the mean absolute deviation (×100) between the averaged and non-averaged distribution is 0.61. For comparison, the respective value for the rotationally symmetrical angular distribution of SSL 1 is 0.04.

The angular intensity curves of SSLs 1, 9, and 12 are presented in Figure 27. The DUTs for the figure were chosen to represent the whole range of beam angles of the measured SSLs. The distribution of SSL 12 measured with Camera 2 was obtained using the alternative reference light source (Reference lamp 2). The sudden drop in the angular intensity distribution of the DUT is caused by the fact that the areas of the opposite hemisphere from the beam center are assumed to be diffuse reflected light. This is a compromise between the accuracy of the estimate of the ambient illuminance and the maximum width of the resolvable radiation patterns.

SSL 12 demonstrated prominent flicker which was manifested as the uneven resolved intensity distribution of the SSL when using Camera 1, which employs a rolling shutter. This adds up to the already considerable deviation between Camera 1 and the goniophotometer caused by the too wide beam angle of SSL 12 when using the original reference light source. The impact of the flicker is more significant on the DUTs with wide beam angles, since the SNR is already worse due to smaller difference between the direct and the reflected illuminance on the inner surface of the sphere.

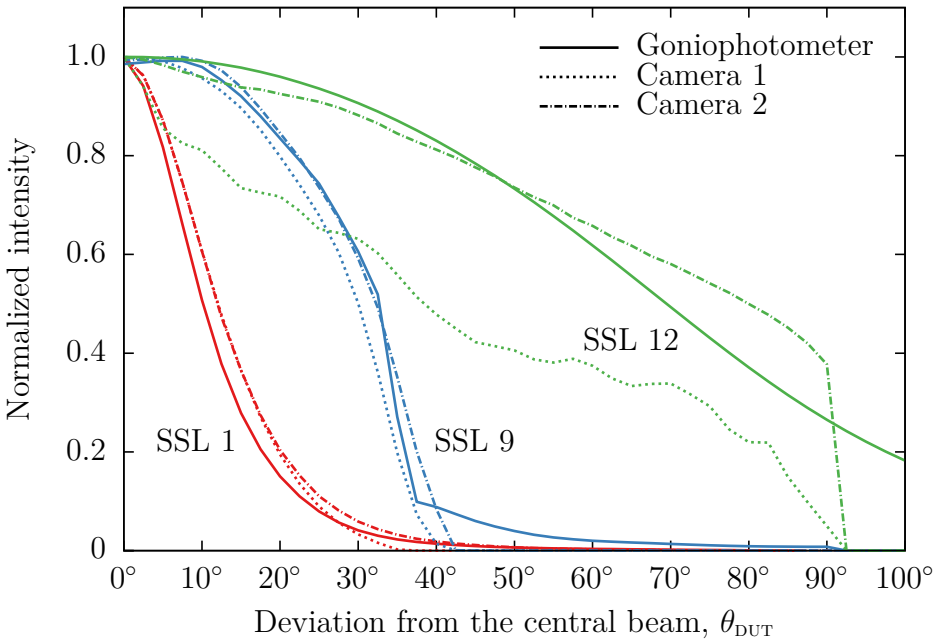

Figure 27: Angular intensity curves of three SSLs with different beam angles.

The angular intensity distributions of all the twelve SSLs are visualized in Appendix B along with their respective goniometrically obtained references for comparison. Data for the appendix was obtained using Camera 2. Distributions of SSL 11 and SSL 12 for the appendix were measured using the alternative reference lamp.

5.3 Analyzed spatial non-uniformity corrections

From the measured relative angular intensity distributions, the impact of the deviations on the spatial correction was studied using the scanned SRDF of the integrating sphere shown in Figure 3. For an SSL with a perfectly uniform angular intensity distribution, the spatial correction factor k_{s} for this system would be 1.00145. Because of the direct proportionality, the deviations in spatial correction factors are directly seen in the luminous efficacies determined for DUTs. The calculated spatial correction factors for the twelve measured SSLs are presented in Table 4. The factors obtained using both cameras are based on the measurements carried out with the reference light source show in Figure 22. The values for Table 4 are calculated ignoring the detected pointing direction of the DUT in order to facilitate the comparison between the two methods. The central beam of all lamps was assumed to be towards the bottom of the sphere at $\theta = 180°$. The relative differences in spatial correction factors for the table were calculated according to

$$\Delta_{\mathrm{ref}} = \frac{\mid k_{\mathrm{s,camera}} - k_{\mathrm{s,reference}} \mid}{k_{\mathrm{s,reference}}} \cdot 100\,\% \tag{30}$$

Table 4: Comparison of the spatial non-uniformity correction factors k_s obtained using the fisheye camera method and the goniophotometer reference

DUT	Beam angle	Reference	Camera 1	Δ_{ref} [%]	Camera 2	Δ_{ref} [%]
SSL 1	21.0°	1.0186	1.0200	0.14	1.0186	0.01
SSL 2	21.0°	1.0142	1.0169	0.27	1.0143	0.01
SSL 3	21.5°	1.0186	1.0219	0.32	1.0215	0.28
SSL 4	28.6°	1.0171	1.0184	0.13	1.0181	0.10
SSL 5	31.4°	1.0210	1.0216	0.05	1.0212	0.01
SSL 6	51.9°	1.0154	1.0150	0.04	1.0161	0.07
SSL 7	55.5°	1.0153	1.0179	0.25	1.0172	0.19
SSL 8	65.1°	1.0149	1.0148	0.01	1.0158	0.09
SSL 9	65.4°	1.0150	1.0167	0.17	1.0162	0.12
SSL 10	80.6°	1.0130	1.0149	0.19	1.0152	0.22
SSL 11	105.4°	1.0099	1.0122	0.23	1.0131	0.32
SSL 12	139.0°	1.0066	1.0087	0.21	1.0090	0.24

There is no clear correlation between the magnitudes of the mean absolute deviations of the relative angular intensity distributions obtained using the two methods and the relative differences in spatial correction factors. Because the correction factor is an integral over an area, it is more sensitive to divergences when measuring the total luminous flux of SSLs with narrow beam angles. Differences in determined intensity distributions for lamps with wide beam angles do not impact the spatial correction factor as significantly. For instance, the mean absolute difference ($\times 100$) of 0.26 in the case of SSL 3 leads to a 0.28 % difference in the correction factor, while the respective value of SSL 12, 8.02, leads to a 0.24 % deviation. This is supported by the differences in calculated correction factors obtained using the two cameras. For wide beam angles of SSLs 10–12, despite the fact that the mean absolute differences for the angular intensity distributions obtained using Camera 2 were smaller than the ones for Camera 1, the deviations of the correction factors are the other way around.

For SSL 11 and SSL 12 using Camera 2 and the alternative reference light source leads to correction factors 1.00957 and 1.00738, respectively. Subsequently, the relative differences compared to the goniophotometer become 0.03 % for SSL 11 and 0.08 % for SSL 12. Because the angular intensity distribution of SSL 12 extends beyond $\theta_{DUT} = \pm 90°$, the spatial non-uniformity correction factor for SSL 12 approaches the smallest resolvable correction using the developed fisheye camera method. The limit is caused by the assumption that the illuminance of opposite hemisphere from the beam center is the diffuse illuminance level inside the integrating sphere. For any smaller factors, an assumption of isotropic distribution ($k_s = 1.00145$) leads to a relative deviation of less than 0.59 % in the spatial correction factor.

For the measured SSLs, ignoring the spatial non-uniformity correction altogether

would lead to a maximum of 2.1 % deviation in the measured luminous flux compared to the corrected value using the goniophotometer. Using the factor for a perfectly uniform hemispherical angular intensity distribution with a central beam at the bottom of the sphere ($k_\mathrm{s} = 1.00597$) would still lead to a 1.47 % difference for SSL 5, which requires the largest spatial correction.

The lamp holder of the integrating sphere used in the measurements is not parallel to the zenith angle $\theta = 180°$ and it may also be mounted at different ϕ angles. Additionally, the optical axes of some of the measured DUTs deviate noticeably from the mechanical axes of their E27 screw bases. The heading of the optical axis of the DUT is resolved when using the fisheye camera method, and may also be applied when calculating the spatial non-uniformity correction. When using a goniometer to obtain the angular distribution of a DUT, additional measurements are required to determine the heading of the optical axis inside the integrating sphere.

5.4 Uncertainty analysis

The expanded uncertainty ($k = 2$) of the spatial non-uniformity correction determined using the fisheye camera method is 0.28 %. The uncertainty was obtained using Monte Carlo simulations. The Monte Carlo method is based on modelling the measurement setup and repeating the simulation of the measurement procedure by including both random and biased types of errors [37]. The simplified uncertainty budget for the fisheye camera method is presented in Table 5. The combined relative uncertainty was determined by simultaneously including all sources of uncertainty in the simulation. The impact of an individual source was determined by excluding it from the simulation, and inspecting the change in the total uncertainty simulated with all the components included.

Table 5: The uncertainty budget of spatial non-uniformity correction factor k_s obtained using the fisheye camera method

Source of uncertainty	$100 \times$ relative uncertainty
Reference lamp	0.14
Camera	< 0.01
Extrinsic parameters	
Intrinsic parameters	
Projection function	
Other factors	< 0.01
DUT pose	
SRDF	
Central beam detection	
Combined standard uncertainty	0.14
Expanded uncertainty ($k = 2$)	0.28

The greatest impact of all the uncertainty components comes from the utilized reference lamp. The method heavily relies on the uniformity of the reference light source at the angles where the angular intensity distribution of the DUT is non-zero. Non-uniform reference light sources have the largest impact on the spatial correction coefficients of SSLs with concentrated intensity distributions.

The standard deviations of the pitch, yaw, and roll ($0.35°, 0.53°$, and $0.36°$ respectively) of the camera for the simulation were determined by capturing several images of the integrating sphere, illuminated by different nearly omnidirectional light sources, and letting the measurement software to estimate the camera pose. The actual pose of the camera was kept unchanged. The uncertainties for the intrinsic parameters of the camera were given by the used calibration software.

The standard deviation of the SRDF for the simulation was calculated from the raw measurement data of the commercial sphere scanner. The bottom of the integrating sphere and the spot on the sphere wall $(\theta_{\text{ref}}, \phi_{\text{ref}})$ where the luminous flux from the external source has its first reflection were rescanned after each $\Delta\phi$ step to take into account the stability and the positioning repeatability of the sphere scanner [7]. The standard deviation of the scan and the value used for the simulation was 0.002.

Because the rotation of the DUT is automatically detected from the image, and it is possible to verify the accuracy of the detection from the reconstructed sphere, the standard deviation for the detected pose of the DUT for the simulation was set to $1°$ in all directions. This value affects both the accuracy of the resolved angular intensity distribution and the subsequent pointing direction of the optical axis of the DUT.

The combined standard uncertainty of the spatial non-uniformity correction factor obtained using the fisheye camera method is of the same order as using the goniophotometer at the MRI, 0.1 % [9]. The uncertainty of goniometric measurements is mainly caused by the alignment and the stability of the DUT. For the fisheye camera method, the combined standard uncertainty could be reduced by finding and employing a reference light source which would have as uniform angular intensity distribution as possible.

6 Conclusions

In this thesis, a fisheye camera method for determining spatial non-uniformity corrections for SSL products in luminous flux measurements with integrating spheres was presented. The developed method is based on resolving the relative angular intensity distribution of the device under test from an image taken through the detector port of the integrating sphere using a fisheye lens camera. The method does not require any modifications to the integrating sphere.

To validate the developed method and software, the relative angular intensity distributions of twelve SSLs were measured using the fisheye camera method and compared to the respective goniophotometer reference. To determine the influence of the employed imaging hardware, two fisheye cameras of different price ranges, were used for the validation. The impact of the deviations in the measured intensity distributions on the spatial non-uniformity correction factor, and thus on the luminous efficacy, was studied.

The validation of the method showed that the fisheye camera method is able to relatively accurately resolve the intensity distributions of SSLs whose radiation patterns were within the uniform angular intensity range of the reference lamp. The spatial corrections determined for DUTs with wider beam angles deviated more from the goniophotometer reference due to the intensity fall-of at angles over 60° of the reference lamp used in the calibration of the fisheye camera with a sphere. However, by substituting the reference light source with a lamp having a broader, albeit more inconsistent intensity distribution, the deviations of relative angular distributions of DUTs with wide beam angles were reduced.

For lamps with narrow beam angles, the differences between the industrial and the consumer grade cameras were insignificant. Despite the averaging image capturing method, the most prominent difference between the cameras came from the differing shutter techniques which affected the measurements of flickering DUTs with wide beam angles. The images captured with the industrial grade camera were less prone to the flicker of the SSLs because of the global shutter of the camera, compared to the rolling shutter of the consumer grade camera. Since the determination of the spatial correction factor is more susceptible to deviations in concentrated intensity distributions, the resulting relative differences in the correction factor between the cameras did not increase along with the beam angles. The deviations in spatial non-uniformity correction factors between the goniophotometer and the fisheye camera method ranged from 0.01 to 0.32 % for both cameras.

The expanded uncertainty ($k = 2$) of the spatial non-uniformity correction factors obtained using the fisheye camera method is 0.28 %. The most significant source of the measurement uncertainty is the non-uniformity of the utilized reference lamp. This is because the method is based on the assumption of the uniform angular intensity distribution of the reference light source, which is difficult to accurately

achieve in practice. A possibility of applying a correction to the angular distribution of the reference lamp or finding, or virtually creating, a close-to-uniform reference light source needs to be studied.

Despite the higher uncertainty in the spatial correction compared to the traditional goniometric measurements, the fisheye camera method is a viable alternative for industrial test laboratories due to its less time and resource intensive nature. The measurement procedure for one SSL using the fisheye camera method took minutes, compared to six to seven hours using the goniophotometer. For the measured SSLs, entirely ignoring determination of the spatial non-uniformity correction factor would, at worst, lead to a 2.1 % error of the measured total luminous flux, and correspondingly the luminous efficacy.

References

[1] Y. Ohno, "Detector-based luminous-flux calibration using the Absolute Integrating-Sphere Method," *Metrologia* **35**, 473 p. (1998).

[2] Y. Zong, "Development of a new sphere-goniophotometer method," in *Proc. - 28th CIE Sess. 2015 - Abstr.*, 147 p., 2015.

[3] CIE S 017/E:2011, *ILV: International Lighting Vocabulary,* (International Commission on Illumination, Vienna, Austria, 2011) 173 p.

[4] J. Hovila, P. Toivanen and E. Ikonen, "Realization of the unit of luminous flux at the HUT using the absolute integrating-sphere method," *Metrologia* **41**, 407 p. (2004).

[5] M. L. Rastello, E. Miraldi and P. Pisoni, "Luminous-flux measurements by an absolute integrating sphere," *Appl. Opt.* **35**, 4385–4391 (1996).

[6] Y. Ohno, M. Lindemann and G. Sauter, "Analysis of integrating sphere errors for lamps having different angular intensity distributions," *J. Illum. Eng. Soc.* **26**, 107–114 (1997).

[7] J. Askola, "Characterization of an integrating sphere setup for measurements of organic LEDs," Aalto University, School of Electrical Engineering, Master's thesis, 48 p. (2015).

[8] Y. Ohno and R. O. Daubach, "Integrating sphere simulation on spatial non-uniformity errors in luminous flux measurement," *J. Illum. Eng. Soc.* **30**, 105–115 (2001).

[9] T. Poikonen, T. Pulli, A. Vaskuri, H. Baumgartner, P. Karha and E. Ikonen, "Luminous efficacy measurement of solid-state lamps," *Metrologia* **49**, S135–S140 (2012).

[10] J. Kannala and S. Brandt, "A generic camera model and calibration method for conventional, wide-angle, and fish-eye lenses," *IEEE Trans. Pattern Anal. Mach. Intell.* **28**, 1335–1340 (2006).

[11] F. Devernay and O. Faugeras, "Straight lines have to be straight," *Mach. Vis. Appl.* **13**, 14–24 (2001).

[12] V. Orekhov, B. Abidi, C. Broaddus and M. Abidi, "Universal camera calibration with automatic distortion model selection," in *Proc. - Int. Conf. Image Process. ICIP*, vol. 6, 397–400, 2007.

[13] G. Xu, J.-i. Terai and H.-Y. S. H.-Y. Shum, "A linear algorithm for camera self-calibration, motion and structure recovery for multi-planar scenes from two perspective images," in *Proc. - IEEE Conf. Comput. Vis. Pattern Recognit.*, vol. 2, 2000.

[14] K. Miyamoto, "Fish eye lens," *J. Opt. Soc. Am.* **54**, 1060 p. (1964).

[15] J. Courbon, Y. Mezouar, L. Eck and P. Martinet, "A generic fisheye camera model for robotic applications," in *Proc. - IEEE Int. Conf. Intell. Robot. Syst.*, vol. 1, 1683–1688, 2007.

[16] R. Tsai and Tsai, "A versatile camera calibration technique for high-accuracy 3D machine vision metrology using off-the-shelf TV cameras and lenses," *IEEE J. Robot. Autom.* **3**, 323–344 (1987).

[17] C. Hughes, P. Denny, E. Jones and M. Glavin, "Accuracy of fish-eye lens models.," *Appl. Opt.* **49**, 3338–3347 (2010).

[18] J. J. Kumler and M. L. Bauer, "Fisheye lens designs and their relative performance," *Int. Soc. Opt. Photonics* **4093**, 360–369 (2000).

[19] D. Schneider, E. Schwalbe and H. G. Maas, "Validation of geometric models for fisheye lenses," *ISPRS J. Photogramm. Remote Sens.* **64**, 259–266 (2009).

[20] Ailipu Technology Co. Ltd, *ELP-USBFHD01M-L180*, Device datasheet

[21] IDS Imaging Development Systems GmbH, *UI-1251LE-C-HQ*, Device datasheet

[22] Lensation, *Lensagon BF2M15520*, Device datasheet

[23] P. D. Coates and I. M. Ward, "The plastic deformation behaviour of linear polyethylene and polyoxymethylene," *J. Mater. Sci.* **13**, 1957–1970 (1978).

[24] S. Shah and J. K. Aggarwal, "Intrinsic parameter calibration procedure for a (high-distortion) fish-eye lens camera with distortion model and accuracy estimation," *Pattern Recognit.* **29**, 1775–1788 (1996).

[25] J. Weng, P. Coher and M. Herniou, "Camera calibration with distortion models and accuracy evaluation," *IEEE Trans. Pattern Anal. Mach. Intell.* **14**, 965–980 (1992).

[26] C. Hughes, M. Glavin and E. Jones, "Simple fish-eye calibration method with accuracy evaluation," *Electron. Lett. Comput. Vis. Image Anal.* **10**, 54–62 (2011).

[27] J.-Y. Bouguet, *Camera Calibration Toolbox for Matlab,* (Computational Vision, California Institute of Technology, 2004)

[28] E. Valenza, *Blender 2.6 Cycles: Materials and Textures Cookbook,*, 1st Edition (Packt Publishing Ltd, Birmingham, 2013) 265 p.

[29] M. N. Inanici, "Evaluation of high dynamic range photography as a luminance data acquisition system," *Light. Res. Technol.* **38**, 123–136 (2006).

[30] R. O. Duda and P. E. Hart, "Use of the Hough transformation to detect lines and curves in pictures," *Commun. ACM* **15**, 11–15 (1972).

[31] A. Kitanov, S. Bisevac and I. Petrovic, "Mobile robot self-localization in complex indoor environments using monocular vision and 3D model," in *Proc. - 2007 IEEE/ASME Int. Conf. Adv. Intell. mechatronics*, 1–6, 2007.

[32] G. S. Robinson, "Color edge detection," *Opt. Eng.* **16**, 479–484 (1977).

[33] J. Seibert, J. Boone and K. Lindfors, "Flat-field correction technique for digital detectors," in *Proc. SPIE - Int. Soc. Opt. Eng.*, vol. 3336, 348–354, 1998.

[34] M. Alchin, *Pro Python – Advanced coding techniques and tools*, 1st Edition (Apress, New York City, 2010) 341 p.

[35] S. van der Walt, S. Colbert and G. Varoquaux, "The NumPy array: A structure for efficient numerical computation," *Comput. Sci. Eng.* **13**, 22–30 (2011).

[36] I. Culjak, D. Abram, T. Pribanic, H. Dzapo and M. Cifrek, "A brief introduction to OpenCV," in *MIPRO, 2012 Proc. 35th Int. Conv.*, 1725–1730, 2012.

[37] N. Metropolis and S. Ulam, "The Monte Carlo Method," *J. Am. Stat. Assoc.* **44**, 335–341 (1949).

A Engineering drawing of the camera adapter

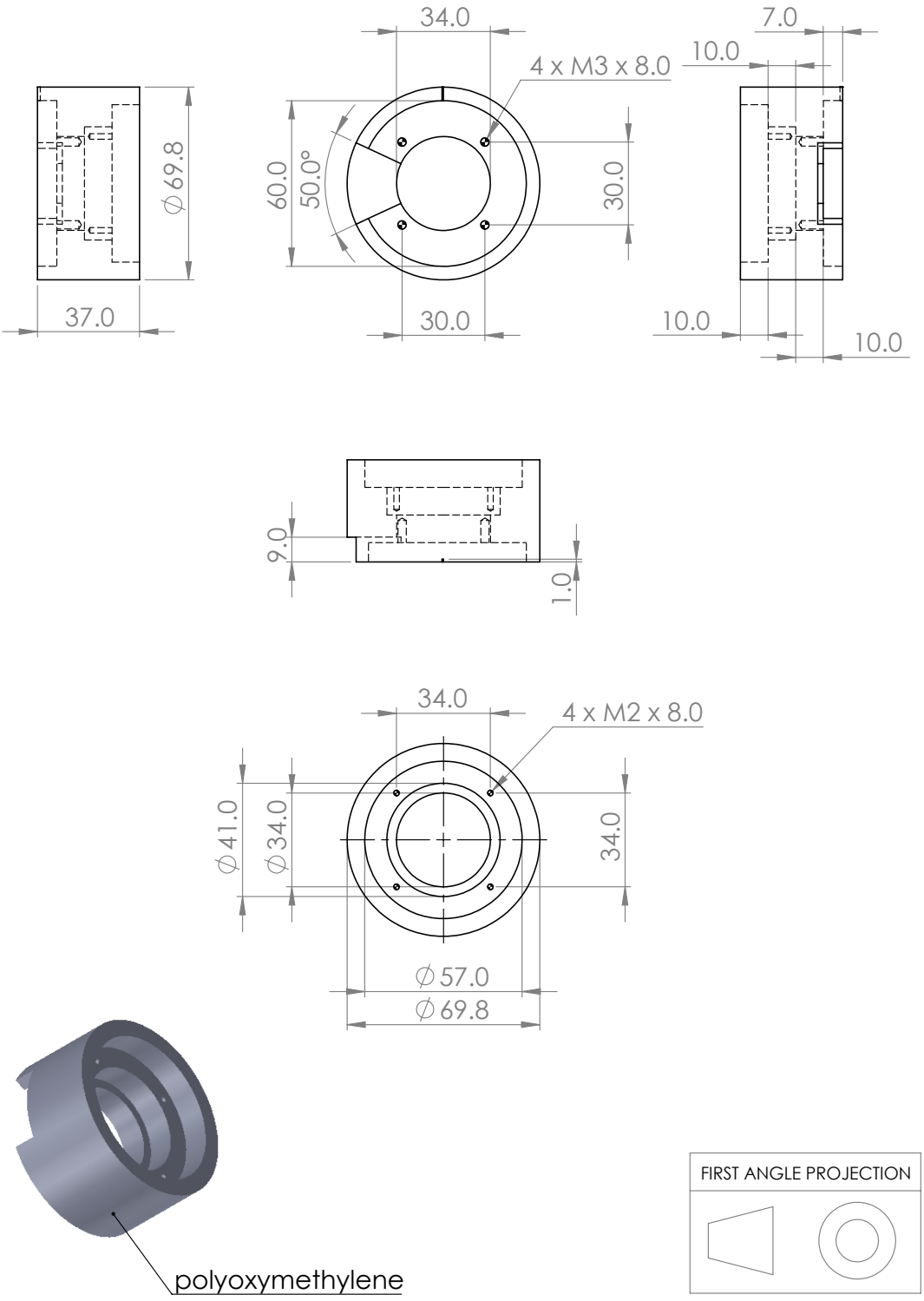

B Angular intensity distributions of the measured SSLs

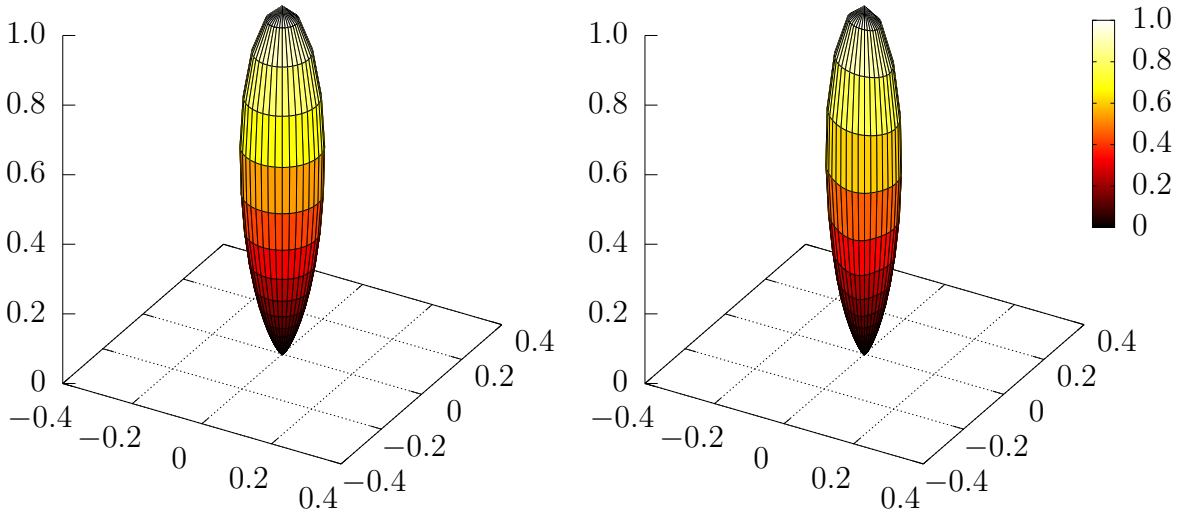

(a) Fisheye camera method

(b) Goniophotometer

Figure B1: SSL 1.

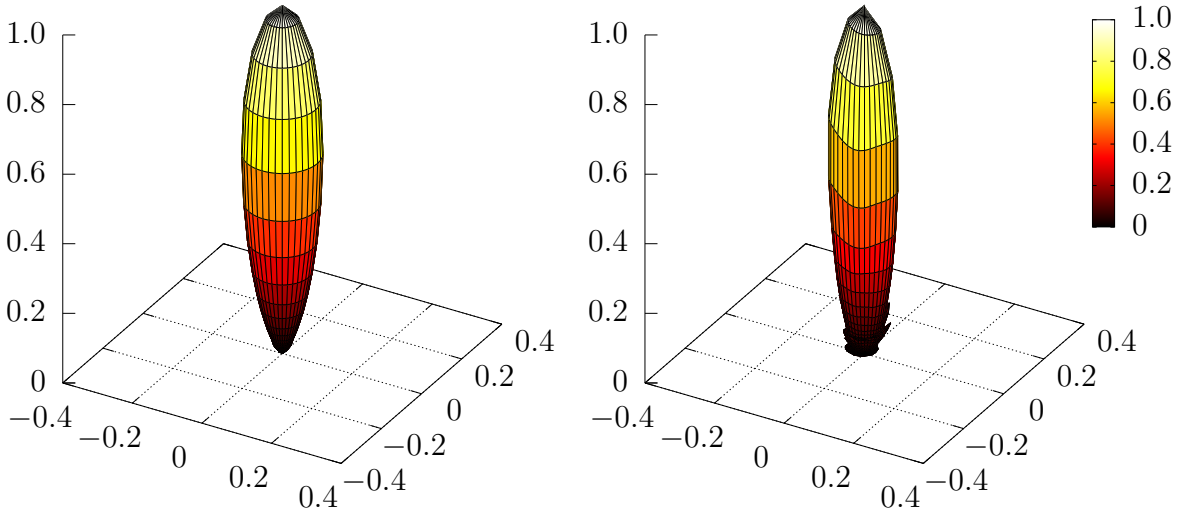

(a) Fisheye camera method

(b) Goniophotometer

Figure B2: SSL 2.

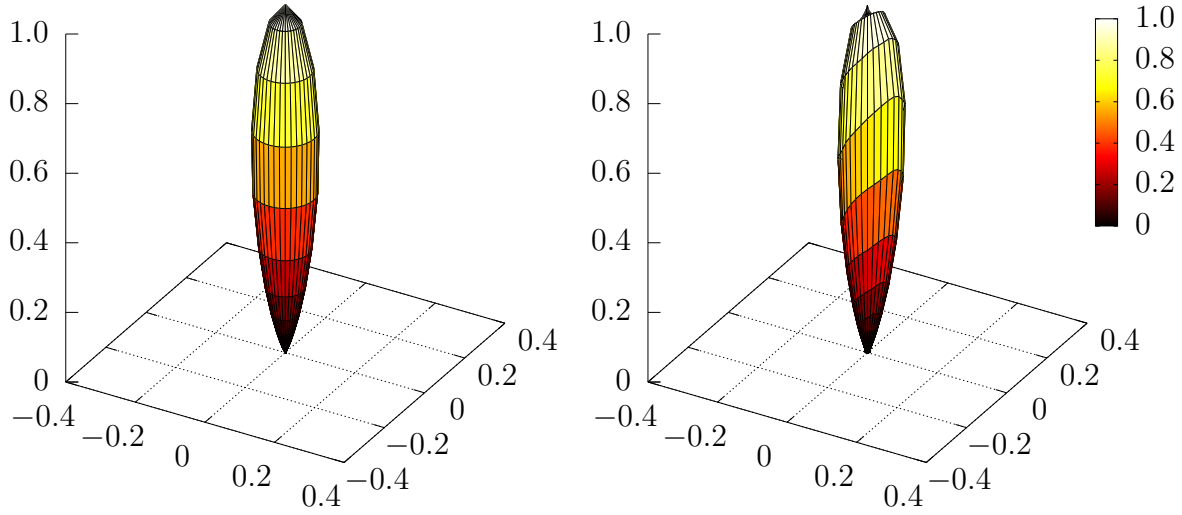

(a) Fisheye camera method (b) Goniophotometer

Figure B3: SSL 3.

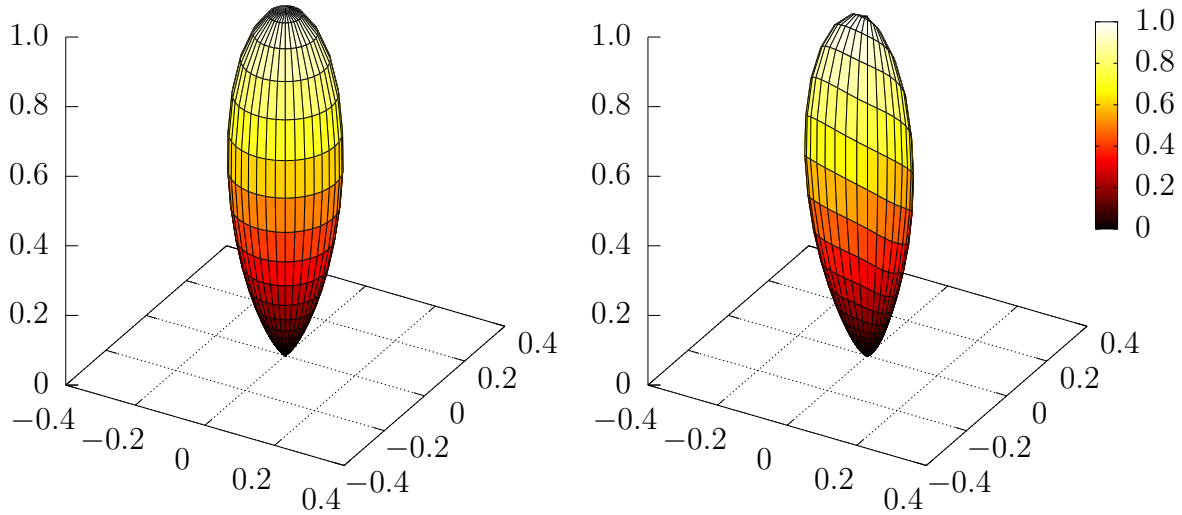

(a) Fisheye camera method (b) Goniophotometer

Figure B4: SSL 4.

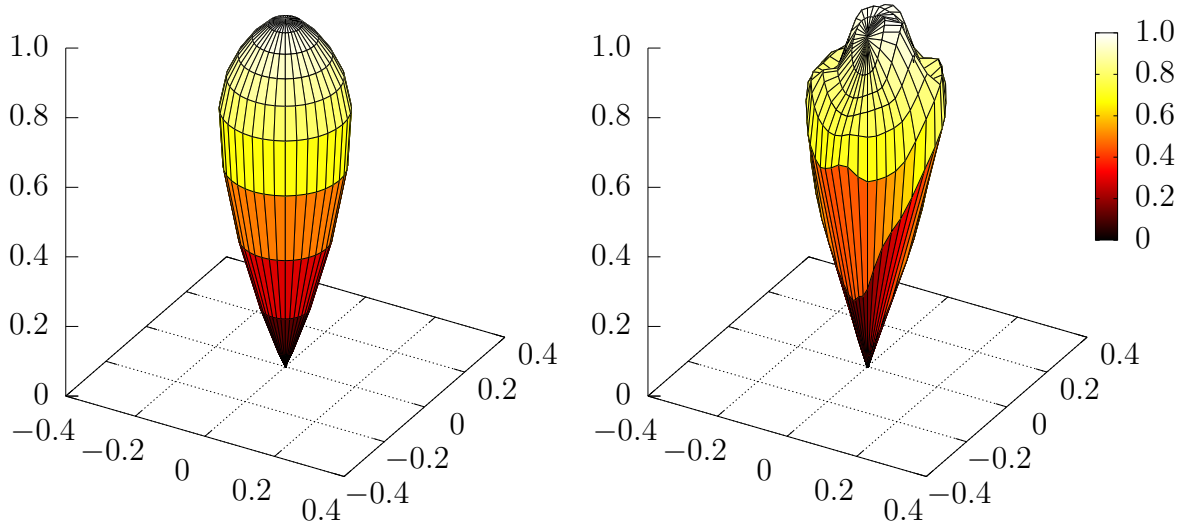

(a) Fisheye camera method (b) Goniophotometer

Figure B5: SSL 5.

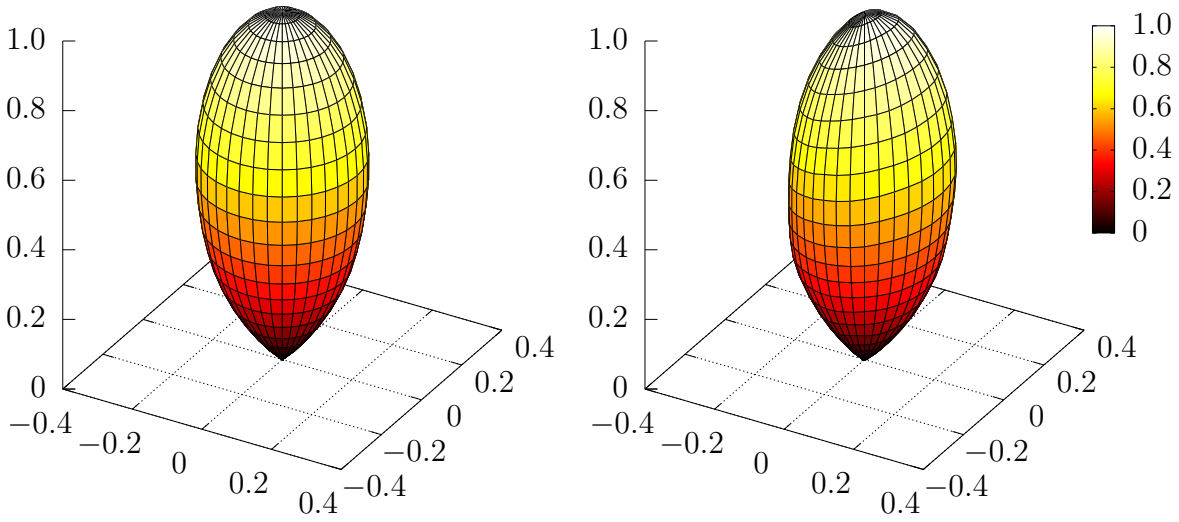

(a) Fisheye camera method

(b) Goniophotometer

Figure B6: SSL 6.

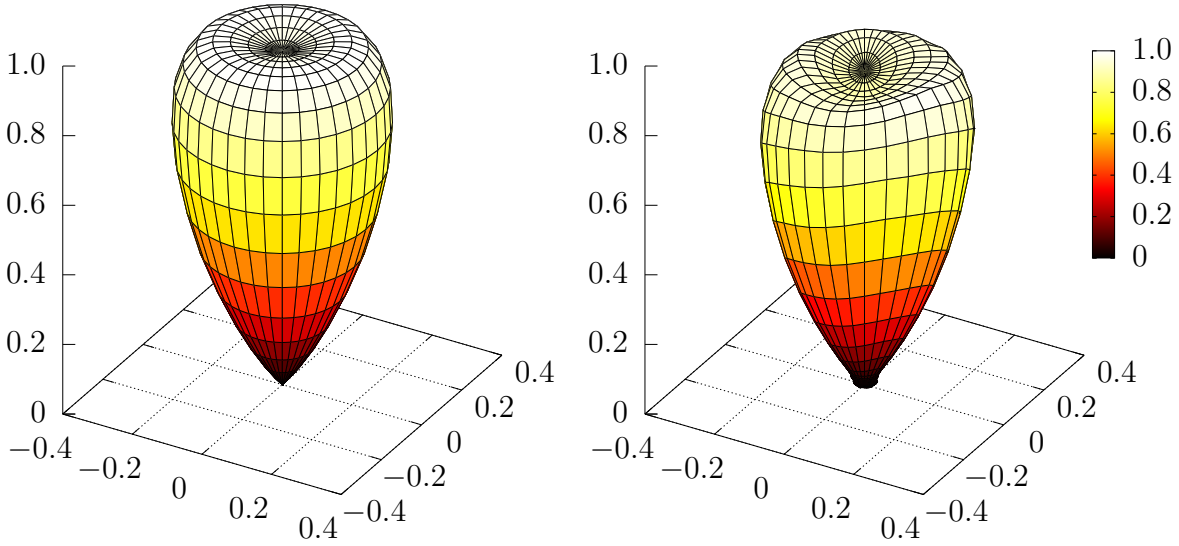

(a) Fisheye camera method

(b) Goniophotometer

Figure B7: SSL 7.

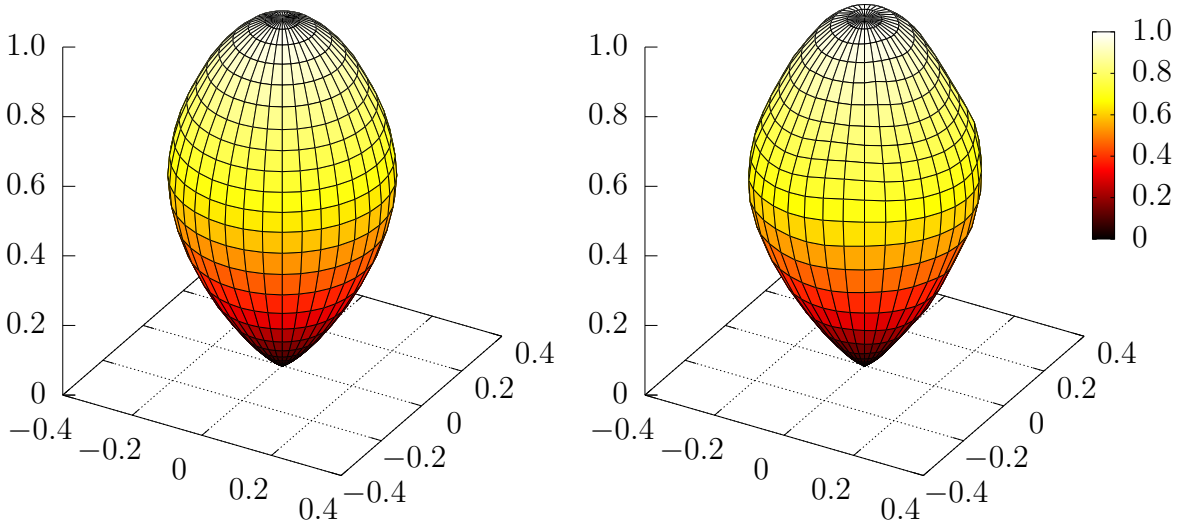

(a) Fisheye camera method

(b) Goniophotometer

Figure B8: SSL 8.

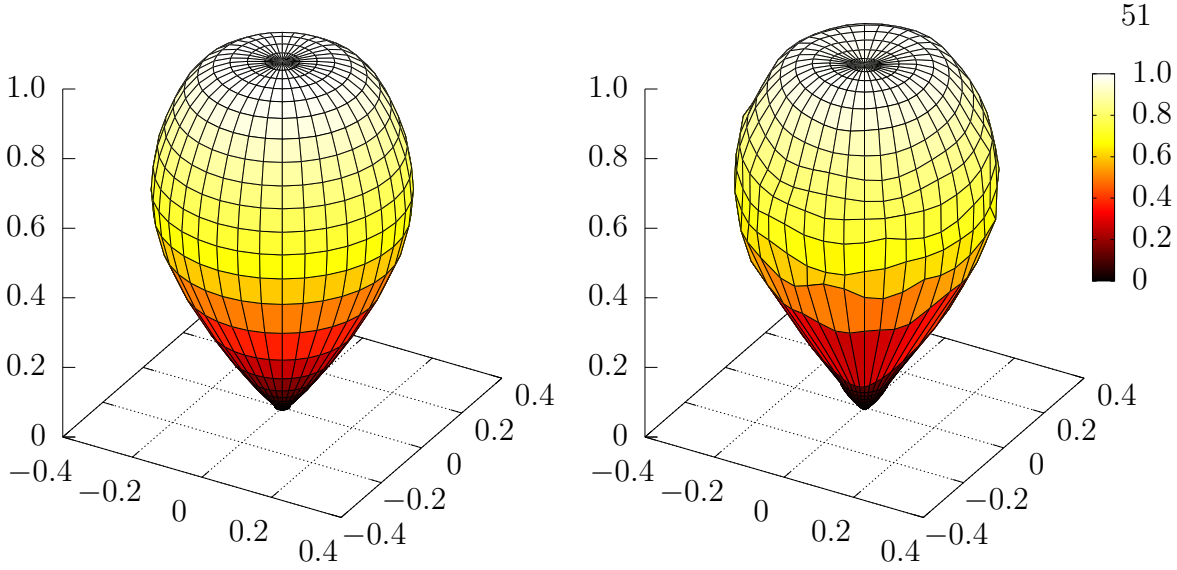

(a) Fisheye camera method

(b) Goniophotometer

Figure B9: SSL 9.

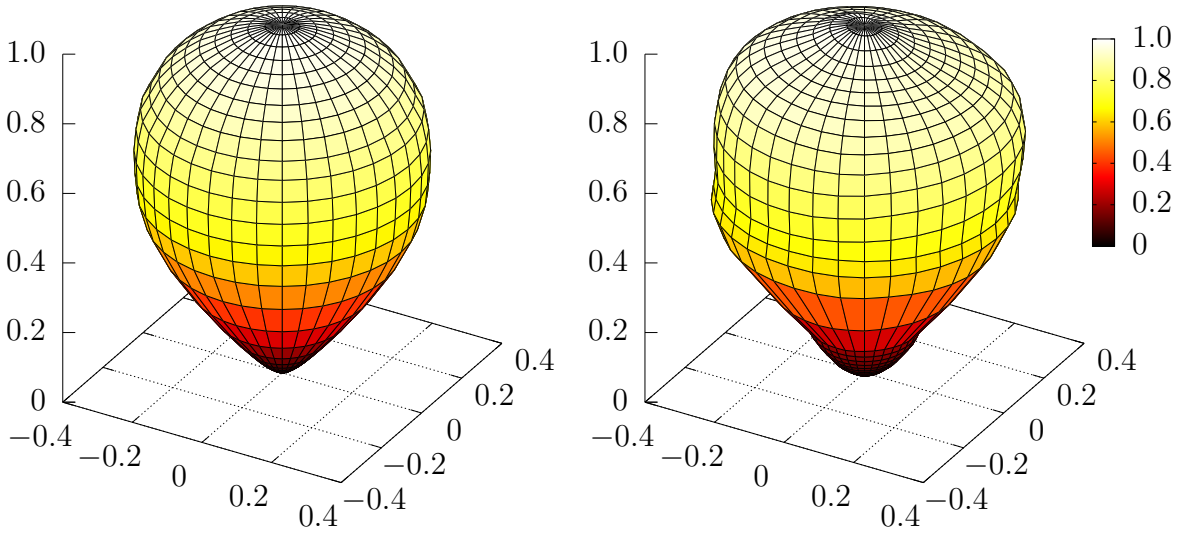

(a) Fisheye camera method

(b) Goniophotometer

Figure B10: SSL 10.

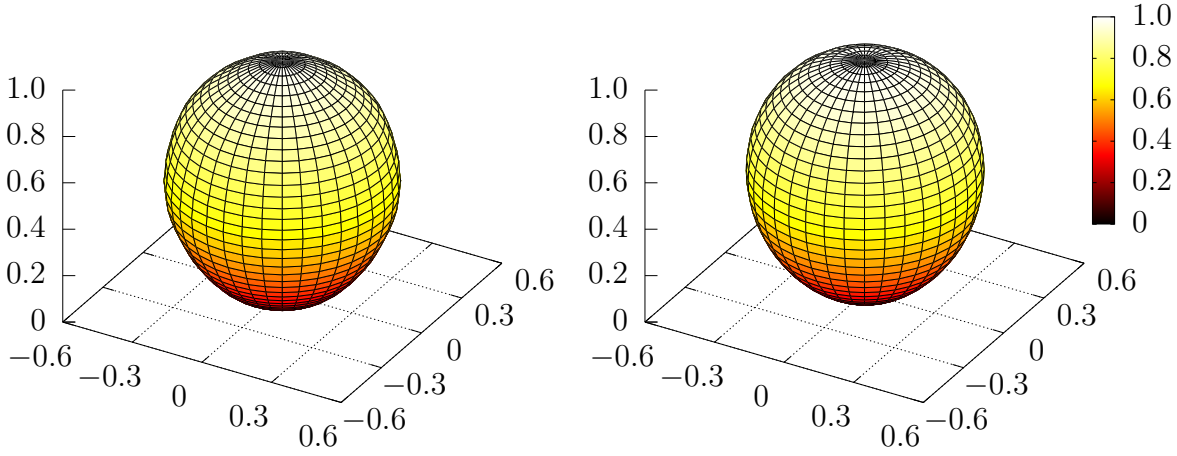

(a) Fisheye camera method

(b) Goniophotometer

Figure B11: SSL 11.

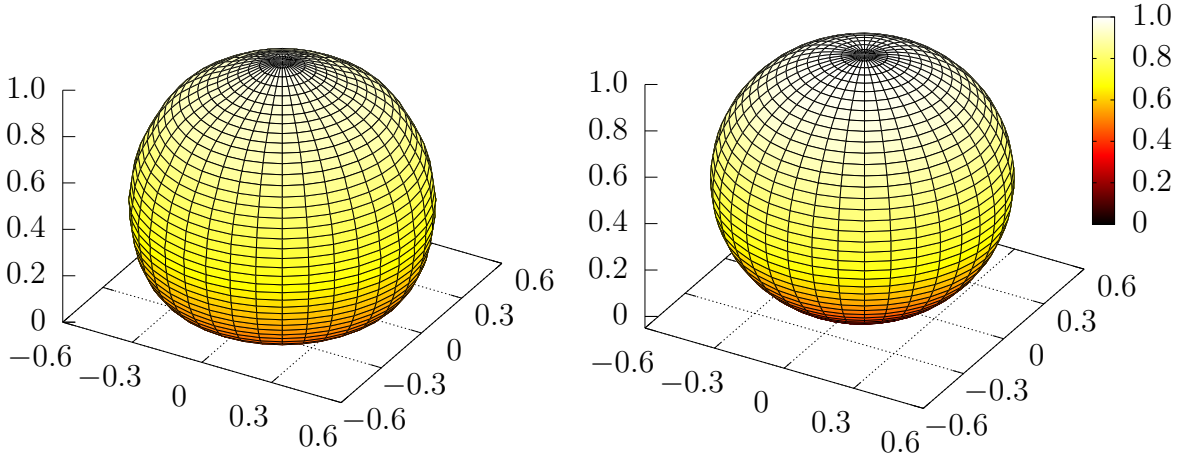

(a) Fisheye camera method

(b) Goniophotometer

Figure B12: SSL 12.